

# Microscopic screening theory for excitons in two-dimensional materials: A bridge between effective models and *ab initio* descriptions

Pedro Ninhos <sup>1,2</sup> Alejandro J. Uría-Álvarez <sup>2,3,4</sup> Christos Tserkezis <sup>1</sup>  
N. Asger Mortensen <sup>1,5</sup> and Juan José Palacios <sup>2,3</sup>

<sup>1</sup>*POLIMA—Center for Polariton-driven Light–Matter Interactions,  
University of Southern Denmark, Campusvej 55, DK-5230 Odense M, Denmark*

<sup>2</sup>*Department of Condensed Matter Physics, Universidad Autónoma de Madrid, 28049 Madrid, Spain*

<sup>3</sup>*Condensed Matter Physics Center (IFIMAC) and Instituto Nicolás Cabrera (INC),  
Universidad Autónoma de Madrid, 28049 Madrid, Spain*

<sup>4</sup>*Departamento de Física, Universidad de Oviedo, 33007 Oviedo, Spain*

<sup>5</sup>*Danish Institute for Advanced Study, University of Southern Denmark, Campusvej 55, DK-5230 Odense M, Denmark*

(Dated: March 2025)

We present a computational approach for exciton calculations in two-dimensional (2D) materials within the Bethe–Salpeter equation (BSE) framework, employing an atomistic description with point-like orbitals. Unlike widespread efficient calculations that rely on classical or effective interaction models, such as the Rytova–Keldysh model, our method incorporates quantum screened interactions. By explicitly computing the 2D dielectric function at the random-phase approximation level, we capture screening effects beyond such approximations with an accuracy akin to first-principles methods. Consequently, we can realistically estimate excitonic binding energies with a bearable computational cost. A detailed account of the various convergence parameters sheds light on a possible cause of the large dispersion of binding energies reported in the literature using first-principles *GW*/BSE implementations. This work thus provides an alternative pathway towards efficient and faithful dielectric screening and exciton computations in low-dimensional materials.

## I. INTRODUCTION

Within a quantum mechanical framework, the optoelectronic properties of solid-state materials can generally be described in terms of electronic excitations from occupied states to higher-energy unoccupied states [1, 2]. In metals or in materials without a bandgap, these transitions between single-particle states are typically intraband in nature when the excitation energies are sufficiently low. In contrast, semiconducting or insulating materials in their ground state require energies typically greater than the single-particle electronic bandgap. Interestingly, the optical response of semiconductors and insulators is non-trivial for frequencies within the range of energies spanning such electronic bandgap [3] where single-particle states are absent. Yet, the system can host quasi-particles known as excitons—bound electron–hole pairs that form at sub-gap energies. This bound state is formally a many-body state; it can only be described when electron–electron interactions are treated beyond the single-particle or mean-field level [4, 5].

Excitons play a central role in determining the optical properties of low-dimensional crystals, such as hexagonal boron nitride (hBN) [6, 7] or transition metal dichalcogenide (TMD) materials [8, 9]. The current interest in excitons within two-dimensional (2D) materials is partly driven by the experimental demonstration of exciton-based light–matter interactions at room temperature [10–12]. Unlike in their three-dimensional (3D) counterpart, excitons in 2D materials are long-lived and have considerable binding energies ranging from a fraction of electron-

volt (eV) to a couple of eV. The large exciton binding energies in 2D materials, compared with those in 3D systems, can be explained by the electrostatic screening being less effective in 2D than in 3D [13]. Due to the reduced dimensionality, the dielectric response of the material essentially affects the electric field lines within it, whereas those off-plane are less affected by the material response. As a consequence, the relative permittivity of a 2D material cannot be described by a single permittivity constant, which poses a challenge from a theoretical standpoint. Somehow, the theory must incorporate the fact that the relative permittivity varies in space and promote it from a constant to a function—the dielectric function. It plays a central role in describing how electric charges inside a material respond to external electric field perturbations within the linear response.

The strong dependence of the dielectric function on space is what confers so-called nonlocal effects to the screening material properties [14]. In other words, the dielectric function in reciprocal space exhibits spatial dispersion with strong dependence on the wavevector. To model this dependence, the analytical Rytova–Keldysh model [15] has been put forward solely on classical grounds, providing an intuitive interpretation for the screened Coulomb potential felt between two electric charges in a 2D crystal. Due to its simple expression in reciprocal space, which follows a linear dependence on the momentum, it offers as well an analytical expression for the Coulomb potential in real space and is widely used in exciton calculations combining analytical with numerical methods [16, 17]. Nonetheless, it has some short-

comings. In the light of classical physics, even though one can predict the behavior of the dielectric function in the low-momentum limit, it is not possible to estimate the model parameter appearing in its formula without the help from quantum mechanics. Moreover, it only captures the screening accurately in the long-wavelength limit. To go beyond that, one has to resort to first-principles methods to obtain the full dependence on momentum. Also called *ab initio* methods, they permit a description of screening and excitons within a single framework, albeit completely computational. This framework relies first on knowledge of the ground state of the system. To date, the most powerful framework for this purpose is density functional theory (DFT) [18, 19], a theory that enables, in principle, the determination of ground state properties of both finite and extended systems based only on the atomic structure under consideration.

Through DFT calculations, we can obtain an approximate single-particle description of the material, on top of which we can do post-processing calculations to obtain the excited states. As DFT usually underestimates the bandgap, before calculating the exciton, this needs to be corrected to bring it closer to the experimental value. The tools of many-body perturbation theory (MBPT) [4, 20] provide a possible way to correct the quasiparticle energies of our many-electron system. The *GW* [21, 22] approximation is one of them, which accounts for dynamical screening and can accurately correct the electronic bandgap. Together with the Bethe–Salpeter equation (BSE) within MBPT, the *GW*+BSE [22–25] method can in one sitting predict the quasiparticle energies and the excitonic levels with great accuracy [22, 23]. Unfortunately, such methods are deemed computationally too heavy. Often, it suffices to extract the numerical macroscopic dielectric function from the DFT calculations, and then fit it to a linear model to recover the Rytova–Keldysh dielectric function. Then, exciton calculations follow, typically by using the BSE on top of a tight-binding description of the material [26–30] or through the effective Wannier equation [31–33]. Nevertheless, despite the extensive literature, there is a methodology gap that the present work aims to fill.

In this manuscript, we explore a middle ground in-between analytical models and *ab initio* descriptions of screening and excitons in 2D extended periodic systems. Taking the reduced dimensionality of the 2D excitonic problem to our advantage, and without compromising a microscopically detailed description of screening, we implement an efficient atomistic description of the microscopic dielectric function based on a strictly 2D formalism. The theory developed herein allows for the evaluation of the full static dielectric response at a much lower computational cost than first-principles methods, capturing both long- and short-wavelength limits (the former being where effective models usually operate). This

is done without an apparent sacrifice of accuracy, since our results match those reported in the *ab initio* literature. Furthermore, the extension of our strict 2D description to a quasi-two-dimensional (Q2D) theory allows for: (i) justifying the zero-thickness approximation done in the strict 2D formalism and investigating its regimes of validity; (ii) improving the dielectric response encoded in the effective macroscopic dielectric function, matching the *ab initio* results of the literature with excellent qualitative and quantitative agreement. All of this, still at a significantly smaller fraction of the computational cost of first-principles methods.

To benchmark and validate our results, we apply the theory and the implementation to two paradigmatic materials, hexagonal boron nitride (hBN) and molybdenum disulfide (MoS<sub>2</sub>). For both materials, we obtain an effective 2D dielectric function rather close to the *ab initio* one, recovering a quantitatively accurate Rytova–Keldysh linear behavior in the long-wavelength limit. As a direct application of our numerically obtained dielectric function (and matrix), we calculate excitonic states through the BSE as implemented in the XATU code [28]. Not only are the results for the exciton energies herein determined compatible with those obtained using first-principles methods, the efficiency of our methodology also allows for a detailed convergence analysis of these energies with the different calculation parameters. Such a complete convergence analysis, including the local-field effects in the interaction kernel of the BSE, is not always feasible, particularly when using *ab initio* calculations due to prohibitive computational costs, and deserves due attention.

## II. RESULTS AND DISCUSSION

### A. Band structure

Excited states of materials are linked to their ground state properties. In an infinite periodic structure, or crystal for short, the single-particle electronic states or Bloch states are typically described by a band index  $n$  and a momentum vector  $\mathbf{k}$ . The set of all quasiparticle electronic energies  $\epsilon_{n\mathbf{k}}$  for every possible  $n$  and  $\mathbf{k}$  constitute the band structure of the material. Even if computed through DFT, the Bloch states  $|n\mathbf{k}\rangle$  and energies  $\epsilon_{n\mathbf{k}}$  commonly constitute a basis for approaching the truly interacting many-body problem. We present first the electronic band structure for two 2D gapped materials, hBN as an insulator and MoS<sub>2</sub> as a semiconductor. Figure 1 displays the band structure of hBN and MoS<sub>2</sub> in panels **a** and **b**, respectively. The band structure of hBN was obtained through DFT calculations with a  $48 \times 48 \times 1$   $\mathbf{k}$ -grid within a framework of localized functions using a Gaussian basis with the commercial package CRYSTAL [34]. For the exchange–correlation functional,

the hybrid functional HSE06 [35] was used, which allows for a much better estimation of the electronic bandgap than using, for instance, the local-density approximation (LDA). CRYSTAL provides the spatial Fock matrices  $H(\mathbf{R})$ , from which we can form the Bloch Hamiltonian  $H(\mathbf{k}) = \sum_{\mathbf{R}} \exp(i\mathbf{k} \cdot \mathbf{R}) H(\mathbf{R})$  that allows for the computation of the quasiparticle energies  $\{\epsilon_{n\mathbf{k}}\}$ , giving a direct bandgap of  $\Delta = 6.08$  eV at the high-symmetry point K in the Brillouin zone (BZ). As explained in Section III B, knowledge of the Bloch Hamiltonian allows as well for the computation of the dielectric function. The lattice constant is  $a = 2.51$  Å, the inter-layer distance used was  $L_{\perp} = 500$  Å, and the Fock matrices are 69 by 69, meaning that in total we have 69 bands for hBN, of which 6 are valence bands and 63 are conduction bands.

The band structure of MoS<sub>2</sub> was obtained similarly, without including spin-orbit coupling (SOC), since we have verified that SOC is irrelevant to compute its screening properties. More specifically, the difference in the matrix elements of the polarizability is seen only in the sixth significant decimal place. The lattice constant for MoS<sub>2</sub> is  $a = 3.16$  Å with the Mo atoms in-plane, and the S atoms with an off-plane displacement of 1.585 Å. The inter-layer distance used was  $L_{\perp} = 500$  Å, and the basis has a size of 62 atomic orbitals, meaning that the Fock matrices are 62 by 62. Therefore, this model has in total 62 bands, of which 23 are valence bands and 39 are conduction bands. This material has the same hexagonal crystalline structure as hBN even though it has three atoms in the unit cell instead of two, and its bandgap of  $\Delta = 2.08$  eV is as well located at the high-symmetry point K in the BZ.

In general, hybrid functionals allow for a very good estimate of the bandgap with lower computational effort than  $GW$  calculations. Nonetheless, as we will observe in Section II C, the calculation of the dielectric function is not grandly affected by the exchange-correlation functional used in the DFT calculations, as our results agree very well with other models in the literature for the same materials with the band structure obtained within LDA.

## B. Polarizability

Before computing the dielectric function matrix elements, one has to ensure that the irreducible non-interacting polarizability that we compute through

$$\chi_{\mathbf{G}\mathbf{G}'}^0(\mathbf{q}) = \frac{2}{N} \sum_{vc, \mathbf{k}\sigma} \frac{I_{c\mathbf{k}, v\mathbf{k}+\mathbf{q}}^{\mathbf{G}} \left( I_{c\mathbf{k}, v\mathbf{k}+\mathbf{q}}^{\mathbf{G}'} \right)^*}{\epsilon_{v\mathbf{k}+\mathbf{q}} - \epsilon_{c\mathbf{k}}} \quad (1)$$

is well converged for any generic momentum  $\mathbf{q}$  in the BZ. Here,  $\sigma$  accounts for spin, the numerator is a product of matrix elements of the form  $I_{n\mathbf{k}, n'\mathbf{k}'}^{\mathbf{G}} \equiv \langle n, \mathbf{k} | e^{-i(\mathbf{k}' - \mathbf{k} + \mathbf{G}) \cdot \mathbf{r}} | n', \mathbf{k}' \rangle$ ,  $\mathbf{G}$  and  $\mathbf{G}'$  are generic vectors

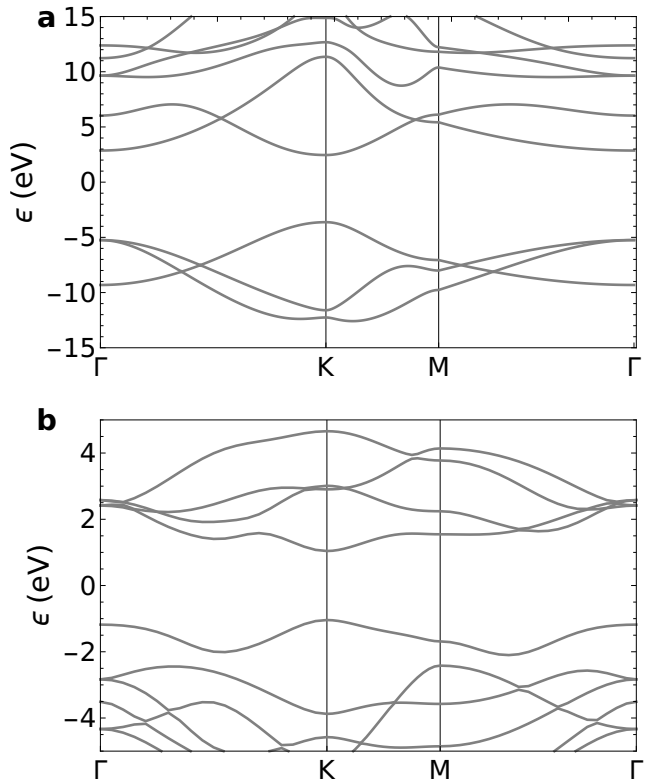


FIG. 1. **Band structures of monolayer hBN and monolayer MoS<sub>2</sub>.** a/b Band structure of monolayer hBN/MoS<sub>2</sub> obtained through DFT calculations, using the exchange-correlation functional HSE06. For both materials, the bandgap is located at the K point of the BZ, and it is  $\Delta = 6.08$  eV for hBN and  $\Delta = 2.08$  eV for MoS<sub>2</sub>. For a better visualization, only the first few bands around the bandgap of each material are displayed.

of the reciprocal lattice,  $v/c$  denotes valence/conduction band, and  $\epsilon_{n\mathbf{k}}$  represents the quasiparticle energies as usual. The sum in momentum  $\mathbf{k}$  is over the whole BZ. Details on the numerical evaluation of this expression are presented in III B. A key approximation in this work is the point-like orbital approximation, where we ignore altogether the spatial details of the atomic orbitals; this allows us to work out an analytical expression for the matrix elements, which can be evaluated numerically without the need of using any additional library to perform fast Fourier transforms (FFTs), and with negligible computational effort.

Although the convergence with the number of points  $N$  in the BZ is not recorded in this manuscript, we have verified that a sparse mesh is sufficient, where only around  $N \sim 17^2$  momentum points ( $\sqrt{N}$  in each direction) are needed, without much difference from material to material. We have also verified the convergence with the number of conduction bands, and the results are displayed in Fig. 2. We test the convergence of the  $\mathbf{G} = \mathbf{G}' = \mathbf{0}$  element of the non-interacting polarizability  $\chi_{\mathbf{0}\mathbf{0}}^0(\mathbf{q})$ , usually

called head element in the literature, as per Eq. (1) with the number of conduction bands included in that sum. Figures 2a and 2b correspond to hBN and MoS<sub>2</sub>, respectively, for a specific  $\mathbf{q} \in \text{BZ}$ . We also tested the convergence of other elements of the non-interacting polarizability matrix (not shown), off-diagonal ones for instance, by checking the convergence of both real and imaginary parts separately (whenever the imaginary part is non-zero).

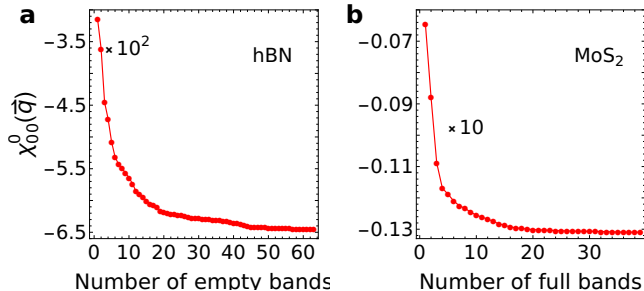


FIG. 2. **Head matrix element of the polarizability.** Convergence of the head matrix element of the non-interacting polarizability with the number of conduction bands included in the sum in Eq. (1). Panel a is for hBN and  $\mathbf{q} = (0.5, 0) \text{ \AA}^{-1}$ , while panel b is for MoS<sub>2</sub> and  $\mathbf{q} = (0.2, 0) \text{ \AA}^{-1}$ . Both polarizability elements are converged with the number of momentum points in the BZ and appear in  $\text{eV}^{-1}$ .

To further validate the calculated polarizability, in Fig. 3 we study the behavior of the  $\chi_{00}^0(\mathbf{q})$  element of the polarizability as a function of  $q = |\mathbf{q}|$ , for both hBN and MoS<sub>2</sub>. Its behavior in the long-wavelength limit  $q \rightarrow 0$  is quadratic as expected. This feature is akin to 2D semiconductors and insulators (also 3D ones, not considered here), and it is universal [36], regardless of the details of the material as long as it presents a bandgap. From one material to another, what changes in the long-wavelength limit is the curvature at the origin (that depends on the direction of  $\mathbf{q}$  if the material is anisotropic). We stress that the polarizability we compute is a strictly 2D one, in the sense that the sum over momentum in Eq. (1) is over in-plane momenta, as the BZ has no off-plane dimensions. The same can be said for the reciprocal lattice vectors, which have no  $z$  component.

Since we have already discussed the results for the polarizability, we are now ready to analyze the dielectric function itself. This is the subject of the next section.

### C. Dielectric function

After the polarizability, we can compute the dielectric function to later study its inverse, which is needed to model the screened interacting potential. Each matrix element of the static dielectric function is obtained

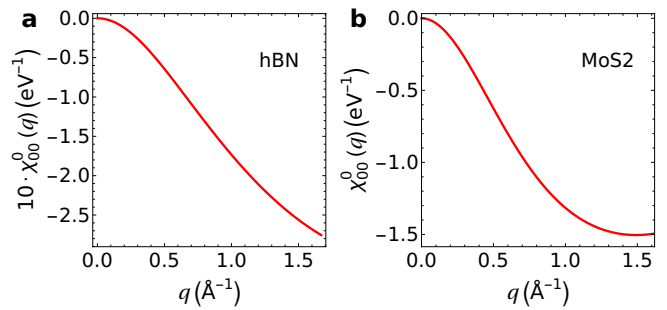


FIG. 3. **Head matrix element of the polarizability as a function of momentum.** Head matrix element of the irreducible polarizability  $\chi_{00}^0(\mathbf{q})$ , as per Eq. (1), as a function of momentum magnitude, for hBN in panel a (scaled by a factor of 10) and for MoS<sub>2</sub> in panel b. The polarizability was computed in both cases along the symmetry line  $\Gamma - \text{K}$ . The momentum  $q = |\mathbf{q}|$  is in  $\text{\AA}^{-1}$  and the polarizability in  $\text{eV}^{-1}$ . Note the different scales for the vertical and horizontal axes in each plot. In both panels, all the valence and conduction bands were included in the sum (1).

through

$$\varepsilon_{\mathbf{G}\mathbf{G}'}(\mathbf{q}) = \delta_{\mathbf{G}\mathbf{G}'} - \sqrt{v_c(\mathbf{q} + \mathbf{G})} \chi_{\mathbf{G}\mathbf{G}'}^0(\mathbf{q}) \sqrt{v_c(\mathbf{q} + \mathbf{G}')}, \quad (2)$$

where the quantity

$$v_c(\mathbf{q}) = \frac{e}{2\varepsilon_0 |\mathbf{q}| \Omega_{\text{UC}}} \quad (3)$$

is the 2D Fourier transform of the Coulomb potential, with  $e$  being the elementary charge,  $\varepsilon_0$  is the vacuum permittivity, and  $\Omega_{\text{UC}}$  the unit cell area. For reasons explained in Sec. III B and also in Section S3 of the Supplementary Information (SI), we have adopted the symmetric representation for the dielectric function. Since what is needed for computing the screened Coulomb potential is the inverse dielectric matrix, we first need to calculate all elements of the direct matrix, and subsequently invert it. In theory, the dielectric function in momentum space has infinite elements. In practice, we have to truncate it for a numerical treatment, since an analytical one is obviously impossible.

Just as typically done in the literature in *ab initio* calculations [37–39], we truncate the dielectric matrix up to a certain maximum cutoff  $G_c^\varepsilon$  for the reciprocal lattice vectors. This means that we include all reciprocal lattice vectors  $\mathbf{G}$  and  $\mathbf{G}'$  such that  $|\mathbf{G}| < G_c^\varepsilon$  and  $|\mathbf{G}'| < G_c^\varepsilon$ , for some value of  $G_c^\varepsilon$ . Even though this cutoff has been explicitly mentioned in the literature in terms of energies, for example in Refs. 37 and 40, at the moment of writing this manuscript we are not aware of any reported study on the convergence of the dielectric matrix with  $G_c^\varepsilon$ , not even in the static limit here considered. Therefore, it is instructive to analyze the convergence of the inverse dielectric function matrix elements  $\varepsilon_{\mathbf{G}\mathbf{G}'}^{-1}(\mathbf{q})$  with the number of vectors  $\mathbf{G}$  included. The detailed discussion of this

issue is done in Section S2 of the SI. In this work, and unlike in Ref. [37], we do not have a single energy cutoff as a convergence parameter for truncating the band structure and the reciprocal lattice simultaneously. Instead, we include a sufficiently large number of empty bands  $N_c$  for the polarizability matrix elements to converge, just as tested in Fig. 2. Afterward, we use the  $G_c^\varepsilon$  parameter for the inclusion of the reciprocal lattice vectors, which is separate from  $N_c$ . If it is converged with the number of conduction bands included in the sum of Eq. (1), then, in principle, convergence of the dielectric matrix and its inverse with a high enough  $G_c^\varepsilon$  is attainable. However, the results shown in Fig. S1 of the SI demonstrate that the convergence of the inverse dielectric matrix with increasing  $G_c^\varepsilon$  is quite slow, which calls for further investigation. More specifically, the convergence of the exciton binding energy with  $G_c^\varepsilon$  must also be tested. However, as we will see next, choosing a small cutoff will be sufficient to compare our results with *ab initio* ones. After the convergence analysis of the inverse dielectric matrix in Section S2 of the SI, the dispersive behavior of the inverse dielectric function is also analyzed.

To finish this section, we discuss the macroscopic effective dielectric function, which can be obtained from our 2D implementation of the microscopic one. For this, we employ the definition

$$\varepsilon_M(\mathbf{q}) = \frac{1}{\varepsilon_{00}^{-1}(\mathbf{q})}, \quad (4)$$

just as usually done in the literature [36, 40, 41]. The results are shown by the continuous red curves in Figs. 4a and 4b, for hBN and MoS<sub>2</sub> respectively. For comparison, we contrast our result with the macroscopic 2D dielectric function obtained from *ab initio* calculations in the literature represented by the continuous black curves. The data for those curves was obtained using the quantum-electrostatic heterostructure (QEH) model from Ref. 42, where the authors developed a Python package for estimating the dielectric properties of van der Waals structures. For the purpose of this manuscript, the QEH package was used for the particular case of monolayer hBN and monolayer MoS<sub>2</sub>.

It is important to note that the data obtained from the QEH Python package are based on previously done first-principles calculations, where the monolayer thickness is naturally incorporated. In the same figure, we present with a blue line the effective 2D dielectric function by taking the monolayer thickness into account. This is possible with the Q2D approach we developed in this work, which is an extension of the strictly 2D one for the dielectric function. In the Q2D approach, the dielectric function has a mixed  $(\mathbf{q}, z)$ -representation, allowing for taking the off-plane degrees of freedom into account. In this way, the monolayer thickness can be included in our

theory. For further technical details, we refer the reader to Section III B 3.

It is worth noting the very good agreement between our curves (in red and blue) and the *ab initio* ones (in black) in the low- $q$  limit. Our implementation constitutes then an efficient method of obtaining the small  $q$ -dependence of the effective 2D dielectric function, which is well captured using a linear model—the so-called Rytova–Keldysh model [15, 43]. The straight black lines in each panel correspond to the Rytova–Keldysh dielectric function for the respective material, which captures the close-to-zero  $q$ -dependence of the dielectric function as  $\varepsilon_{\text{RK}}(q) = 1 + r_0 q$  and its use is widely spread in the literature [14, 16, 17, 30]. The slope  $r_0$  is obtained by fitting the straight curve to the numerical one, and is commonly denoted as screening length or screening parameter [14]. It is also remarkable how well the Q2D approach captures the  $q$ -dependence of the macroscopic dielectric function in the entire  $q$ -range, especially for hBN. Apart from small numerical discrepancies for  $q > 0.5 \text{ \AA}^{-1}$ , the agreement between the black and blue curves is excellent. In the case of MoS<sub>2</sub>, the strict 2D formalism underestimates the *ab initio* screening in overall  $q$ , but approaches it for  $q$  higher than  $2.0 \text{ \AA}^{-1}$ , sensibly. The Q2D approach slightly overestimates the screening with respect to the *ab initio* result around the  $q$  that maximizes  $\varepsilon_M(q)$ , and underestimates it otherwise. But still, the improvement in the overall dielectric response of this material is striking. The gain in using the Q2D approach over the 2D one is more evident for intermediate and higher values of momentum for both materials, namely after the linear approximation breaks down. Nonetheless, we can stress once again the excellent agreement among the three approaches for low values of  $q$ .

From the full dependence of the dielectric function, one can note that for  $q \rightarrow \infty$  the macroscopic dielectric function approaches unity asymptotically, which is a characteristic of the macroscopic dielectric function in 2D (and also 3D) gapped materials [41, 44]. Physically, this means that in the short-wavelength limit the spatial variations of the external potential occur so fast, that the system does not respond to the perturbation and test charges feel a total potential which is just the external potential averaged over a wavelength. With symbols,  $\phi^{\text{total}} = \phi^{\text{ind}} + \phi^{\text{ext}} \approx \phi^{\text{ext}}$  for  $q \rightarrow \infty$ . This is in sharp contrast with the prediction of the Rytova–Keldysh model, for which the external potential is completely screened (due to an extra factor of  $q$  in the denominator, making the total potential scale with  $q$  as  $\phi^{\text{total}} \sim 1/q^2$  instead of  $\phi^{\text{total}} \sim 1/q$ ). The behavior of the *ab initio* dielectric function when  $q \rightarrow \infty$  is well captured by our methods, validating them once more.

One can notice in Fig. 4 that the slope at the origin  $r_0$  for hBN differs significantly from the one for MoS<sub>2</sub>. This parameter can then be seen as an identity of each 2D semiconductor or insulator, as its value depends solely

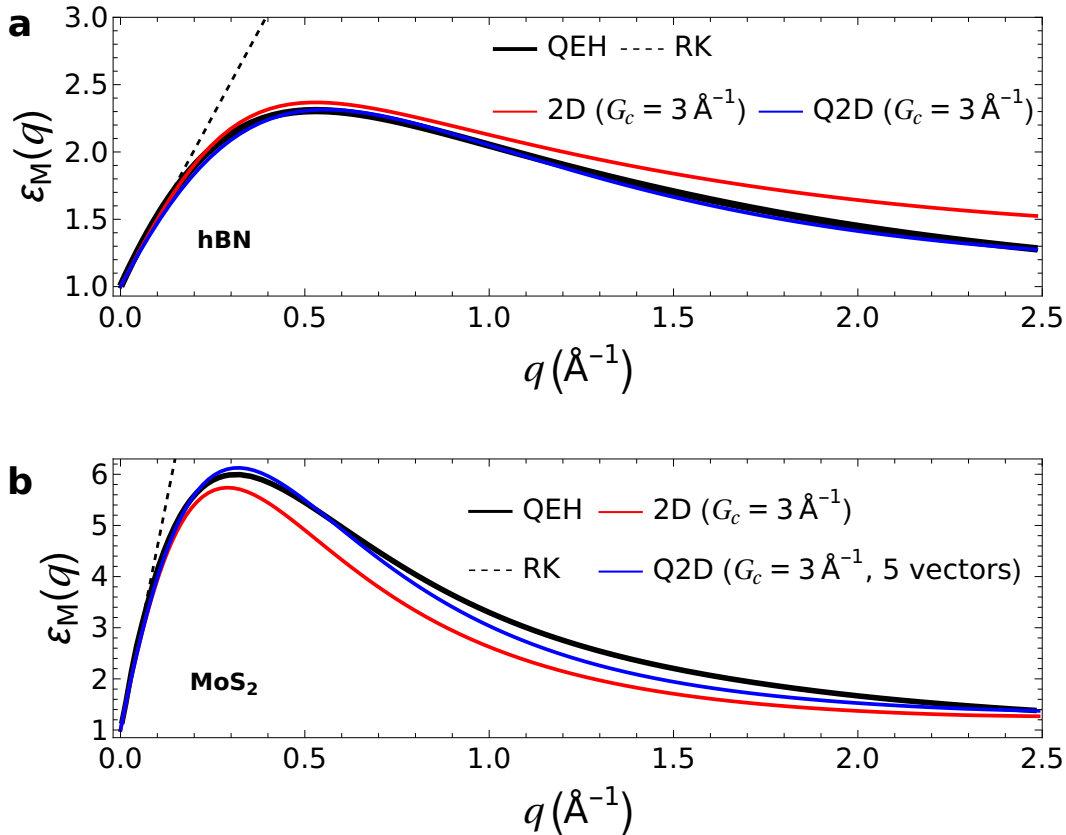


FIG. 4. **Macroscopic dielectric function.** Comparison between the effective 2D dielectric function obtained in this work with *ab initio* methods. Panels **a** and **b** display the results for hBN and MoS<sub>2</sub>, respectively. The *ab initio* results were obtained using the QEHPackage for Python, which can be found in the literature [42], and they are represented by the full black curves. The macroscopic dielectric functions obtained using the strictly 2D description developed in this work as per Eq. (4) are represented in red. The blue curves represent the same quantity, but when obtained through the Q2D approach that we also introduce in this work, explained with detail in Section III B 3. For hBN, in panel **a**, we applied the cutoff  $G_c = 3 \text{\AA}^{-1}$  for the size of the dielectric function. This accounts for seven reciprocal lattice vectors, including the null vector. For MoS<sub>2</sub> we applied the same cutoff, which results in seven  $\mathbf{G}$  vectors as well, but we intentionally discarded two reciprocal lattice vectors in the Q2D approach for the blue curve to better agree with the *ab initio* one. We found that including all vectors underestimated the screening with respect to the black curve. We compare as well the full numerical  $q$ -dependence with the Rytova–Keldysh model in dashed black, with the  $r_0$  parameter estimated by our numerical curves (forcing  $\epsilon_{\text{RK}}(q=0) = 1$ ). For the Q2D results, we used for the monolayer thicknesses the values provided by the QEHPackage for each material.

on the screening properties of the material. As stated above, it is obtained from fitting a straight line to the 2D macroscopic dielectric function in the small  $q$  limit, which one typically gets from first-principles calculations like DFT and DFT+*GW* methods. However, such methods are typically 3D in nature, and the definition (4) cannot be directly applied. First, one has to recover the  $z$ -dependence of the inverse dielectric function (for instance, with the inverse Fourier transform), and only then perform an off-plane average to obtain an effective 2D dielectric function. This process is usually a very heavy computational task.

Within our approach, we can easily estimate the screening parameter by a fit to the macroscopic dielectric function as per Eq. (4), that in our framework is

directly the 2D effective one. This has been confirmed by the results displayed in Fig. 4. We find  $r_0 \approx 5.07 \text{\AA}$  for hBN, and  $r_0 \approx 35.8 \text{\AA}$  for MoS<sub>2</sub>. These values are in very good agreement with the literature. We better show this agreement for hBN in Section S3 of the SI, where we plot our macroscopic dielectric function alongside two other dielectric functions obtained from *ab initio* methods that can be found in the literature. The value obtained for MoS<sub>2</sub> is within the range of values  $r_0 \approx 30 - 40 \text{\AA}$  provided by Ref. 9. Different models may naturally lead to different estimates of this parameter. From inspection of the expression for the polarizability (1), in particular the denominator in the sum, one can expect that the bandgap will affect the outcome of our predictions. Also, the estimated bandgap of a given ma-

terial quantitatively differs from model to model. This aspect is discussed in Section S3 of the SI. Interestingly, the dielectric function that we obtained using a hybrid functional for the DFT calculations is extremely close to the *ab initio* one from Ref. 40, where the band structure was obtained with LDA-DFT (which underestimates the true bandgap). Seemingly, the fine details of the employed Hamiltonian model are not relevant.

It is also important to point out that a more straightforward way of estimating the screening parameter is possible, by directly analyzing the low- $q$  behavior of the (head element of the) microscopic dielectric function. This has been pointed out by Li and Appelbaum in Ref. 45, where they derived an expression for  $r_0$  in terms of an in-plane momentum integral and momentum matrix element between conduction and valence bands, without involving any reciprocal lattice vectors. That expression allowed Quintela *et al.* to estimate in Ref. 46 the value of  $r_0$  for the system therein studied, which was used in the same work for exciton calculations.

The agreement with the *ab initio* results is remarkable, given the simplified nature of our treatment, in the sense that two approximations were made. First, the point-like orbital approximation for the plane-wave matrix elements (explained in detail in Section III B), which does not present any setback. This approximation is advantageous to evaluate the polarizability as per Eq. (1), in which the numerator inside the sum can be computed with negligible computational effort. On the contrary, in *ab initio* approaches where a reciprocal space description of screening is adopted, these matrix elements are typically evaluated through FFTs, implying computational and implementation complications that we avoid altogether. Second, in the strict 2D approach we ignored completely the physics pertaining to the off-plane degrees of freedom. As seen in Fig. 4, this approximation, which we shall discuss more extensively in the Methods section, does not influence the low- $q$  dielectric properties of the material. On the contrary, for intermediate and high values of  $q$ , high enough so that we no longer stand in the linear in  $q$  regime, the strict 2D approach overestimates the screening for hBN and underestimates it for MoS<sub>2</sub>. Fortunately, this penalty in the screening can be fixed by incorporating the non-vanishing monolayer thickness through the Q2D approach for the dielectric function (see Section III B 3).

Once our approach has been validated by comparison with more sophisticated methods, the calculation of the excitonic energies follows as a natural application in the next section.

#### D. Excitons

We devote this section to a convergence analysis of the excitonic states, whilst using our numerical implementa-

tion of the screening in the calculation of the matrix elements of the Bethe–Salpeter Hamiltonian as per Eq. (20). In particular, we use the inverse dielectric matrix to compute the matrix elements of the interaction kernel  $K$  as explained in Section III C. In practice, we discard the exchange term  $X$  and evaluate only the direct term  $D$ , so that  $K = -D$ . Regarding the singular terms that appear in the direct term when  $\mathbf{q} = \mathbf{0}$ , a proper treatment is necessary to avoid numerical errors. Section III C discusses how the head term of the screened potential for zero momentum is regularized, since that is the only one that requires a non-trivial regularization scheme. In brief, we perform an average of the screened potential over a small circular region  $\Omega_\Gamma$  around the origin, just like expressed in Eq. (25). In Section S3 of the SI we argue why the singular terms of the form  $W_{\mathbf{G}\mathbf{0}}$  and  $W_{\mathbf{0}\mathbf{G}}$ , called wing terms, can simply be set to zero. The terms of the form  $W_{\mathbf{G}\mathbf{G}'}$  where  $\mathbf{G} \neq \mathbf{0}$  and  $\mathbf{G}' \neq \mathbf{0}$ , called body terms in the literature, do not need any regularization procedure.

At this stage, a study on how the excitonic binding energies behave with increasing refinement of the BZ,  $N$ , and increasing cutoff for the dielectric function,  $G_c^\epsilon$ , is a natural exercise to do. Due to practical implementations of the singular head element and the double sum over reciprocal lattice vectors for  $D$  in Eq. (24), we have two extra parameters to account for: (i) the radius of the regularization region  $\Omega_\Gamma$ , that we denote by  $q_0$ ; (ii) a cutoff for the reciprocal lattice vectors when calculating  $D$ , that we can denote by  $G_c^X$ . As the parameter space is big, we make two separate convergence studies where we focus on the excitonic ground state. First, we study the convergence of the exciton energy level with  $q_0$  and  $N$  fixing a certain value for the dielectric matrix cutoff  $G_c^\epsilon$ . This time, we include all the reciprocal vectors in  $D$ , i.e., we set  $G_c^X = G_c^\epsilon$ . Second, we fix certain  $q_0$  and  $N$  to study the convergence of the exciton binding energy with  $G_c^\epsilon$  and  $G_c^X$ .

The results of the first convergence study are displayed in Fig. 5 in two sets of four panels, the left ones **a.1** to **d.1** pertaining to hBN and the right ones **a.2** to **b.2** pertaining to MoS<sub>2</sub>. For hBN we set  $G_c^\epsilon = 3 \text{ \AA}^{-1}$ , while for MoS<sub>2</sub> we set  $G_c^\epsilon = 5.1 \text{ \AA}^{-1}$ . In panels **a.1** and **a.2** we plot the energy level of the lowest exciton, denoted by  $E_X$ , as a function of the number of  $\mathbf{k}$  points in the BZ,  $N$ , for different realizations of  $q_0$ . In each realization,  $q_0$  is given by a fraction  $\varsigma$  of the length of the momentum vector closest to the origin, which we denote by  $k_0$ . In both materials, the convergence is slow with  $N$ , with MoS<sub>2</sub> being the worst case. However, plotting  $E_X$  as a function of  $1/\varsigma$  for different realizations of  $N$ , as shown in panels **b.1** and **b.2**, shows that we can model the dependence  $E_X(\varsigma, N)$  with a linear model whose parameters vary among different values of  $N$ . We can thus write  $E_X(\varsigma, N) = m_N \varsigma^{-1} + b_N$ , where  $m_N$  is the slope and  $b_N$  the origin off-set for a given  $N$ . It is evident in panels **b.1** and **b.2** that as we increase  $N$ , the straight line shifts

upwards, and the slope decreases in absolute value. In the limit  $N \rightarrow \infty$  one expects that the line becomes horizontal, meaning that the exciton does not depend on the regularization. This makes sense, since the regularization of the singular terms in the screened potential is a numerical issue—in the limit of an infinite number of  $\mathbf{k}$  points the sum over momentum in Eq. (20) is an integral, and removing a single  $\mathbf{k}$  point in the integration region bears no difference in the final result. Then, the true excitonic energy is the limit  $\lim_{N \rightarrow \infty} b_N$ . To test our hypothesis, we fit a linear model to each curve in panels **b.1** and **b.2**, and obtain the values of the parameters  $m_N$  and  $b_N$  for every realization of  $N$ . Those values are displayed in panels **c** and **d** of each material, respectively. In panels **c.1** and **c.2**, we can clearly see that  $\lim_{N \rightarrow \infty} m_N = 0$  holds for both hBN and MoS<sub>2</sub>. Discussing now the origin off-set, in panel **d.1** we see that  $b_N$  decreases as  $N$  grows. In panel **d.2** we can see that having  $N > 60$  would not bring a significant difference in the value of  $b_N$  for MoS<sub>2</sub>. As a side note, in all the fits that we have performed, the value of  $r^2$  is approximately 1 up to a rounding digit in the fifth decimal place, if not exactly 1.

Continuing our analysis, we take as an estimate for the excitonic energies the values of  $b_{N=60}$  for both materials. For hBN, this means  $E_X \approx b_{N=60} = 3.76$  eV, while for MoS<sub>2</sub> we have  $E_X \approx b_{N=60} = 1.56$  eV. Considering the values of the bandgaps for both materials given in the legend of Fig. 1, the resulting binding energy for hBN is  $E_b = 2.32$  eV. This value is not too distant from *ab initio* ones found in the literature, for instance 2.05 eV in Ref. 40, 1.81 eV in Ref. 47, 2.08 eV in Ref. 48, or, more recently, 1.88 eV in Ref. 49. In the case of MoS<sub>2</sub>, we obtain the binding energy  $E_b = 0.53$  eV, which is also comparable with *ab initio* results. For example, the authors of Ref. 40 obtained therein the value  $E_b = 0.43$  eV, which in turn is rather close to the experimental value of 0.44 eV reported in Ref. 50. As a disclaimer, the analysis performed hitherto was done for a singular value of the cutoff  $G_c^\epsilon$ .

We now compute the excitonic energies while varying the cutoff  $G_c^\epsilon$ , which determines the size of the inverse dielectric matrix incorporated in the interaction matrix element  $D$  in Eq. (24), and the cutoff  $G_c^X$ , which determines the number of terms that appear in the double sum over reciprocal lattice vectors that compose  $D$ . The focus is again the exciton with lowest energy. The results are displayed in Table 6 below. In it, we can identify some patterns worth noting. First, if we consider the first row of each table, for which  $G_c^X = 0$ , and reading the values from left to right, we can see that as  $G_c^\epsilon$  increases, the binding energy also increases. This can be explained by understanding what happens to the 2D effective dielectric function as  $G_c^\epsilon$  increases. It can be seen in Fig. S3 of the SI that the macroscopic dielectric function is overestimated if we include fewer reciprocal lattice vectors in its calculation. Then, as we increase  $G_c^\epsilon$  and

include more vectors  $\mathbf{G}$ , as  $\epsilon_M(\mathbf{q})$  overall decreases, the screened potential given by  $v_c(\mathbf{q})/\epsilon_M(\mathbf{q})$  gets stronger. The attraction between the electron and the hole intensifies, translating into a higher binding energy. Eventually, it grows bigger than the electronic bandgap, which is unphysical (occurs for the entries in the tables with  $> \Delta$ ). To draw conclusions with physical meaning, we must include all  $\mathbf{G}$  vectors when evaluating  $D$ . Doing so, we obtain the results in the diagonal cells of each table. Even though the matrix elements of the inverse dielectric function display a very slow convergence as discussed in Section II C, the binding energy of the exciton seems to converge faster than the inverse dielectric function. These results suggest an important conclusion for calculating excitons through exact diagonalization of the BSE, which was missing until now in the literature—the exciton binding energy converges with the cutoff dielectric function  $G_c^\epsilon$ , albeit slowly. The inclusion of local-field effects, those due to the inhomogeneity of the electron gas in a crystalline solid, into the calculations for both the dielectric and excitonic properties was already a given in the literature [36, 37, 51, 52]. In a semiconductor or insulator these effects cannot be neglected, unlike in the jellium model of the homogeneous electron gas (the continuous translation invariant case) that can be applied to metals up to some extent. However, it was unclear until now in what way do these effects actually influence the results for the macroscopic dielectric function and the excitons, and how these two interplay.

We have seen how the macroscopic dielectric function can be estimated upon a truncation of the microscopic 2D dielectric function up to some cutoff for the reciprocal lattice vectors, with its subsequent inversion. Even though our methods have been validated with great accuracy in comparison with *ab initio* methods, there are no experimentally measured static dielectric functions to compare with and settle the debate.

Despite the apparent convergence of the binding energy in Table 6 below, the possibility of achieving a satisfying convergence in practice is not evident. However, in theory the binding energy has to converge to a single value. This slow convergence may be due to the slow decay of the 2D Coulomb potential. Most likely, these issues are not as problematic as in bulk 3D materials, where  $v_c(\mathbf{q}) \sim 1/q^2$ . To test these hypothesis, one could implement a 3D version of our 2D framework, and treat both types of materials on identical grounds.

### III. METHODS

#### A. DFT calculations

To treat the many-particle problem at the interacting level, one is posed with the problem of choosing an appropriate state basis to work with. Quite commonly in

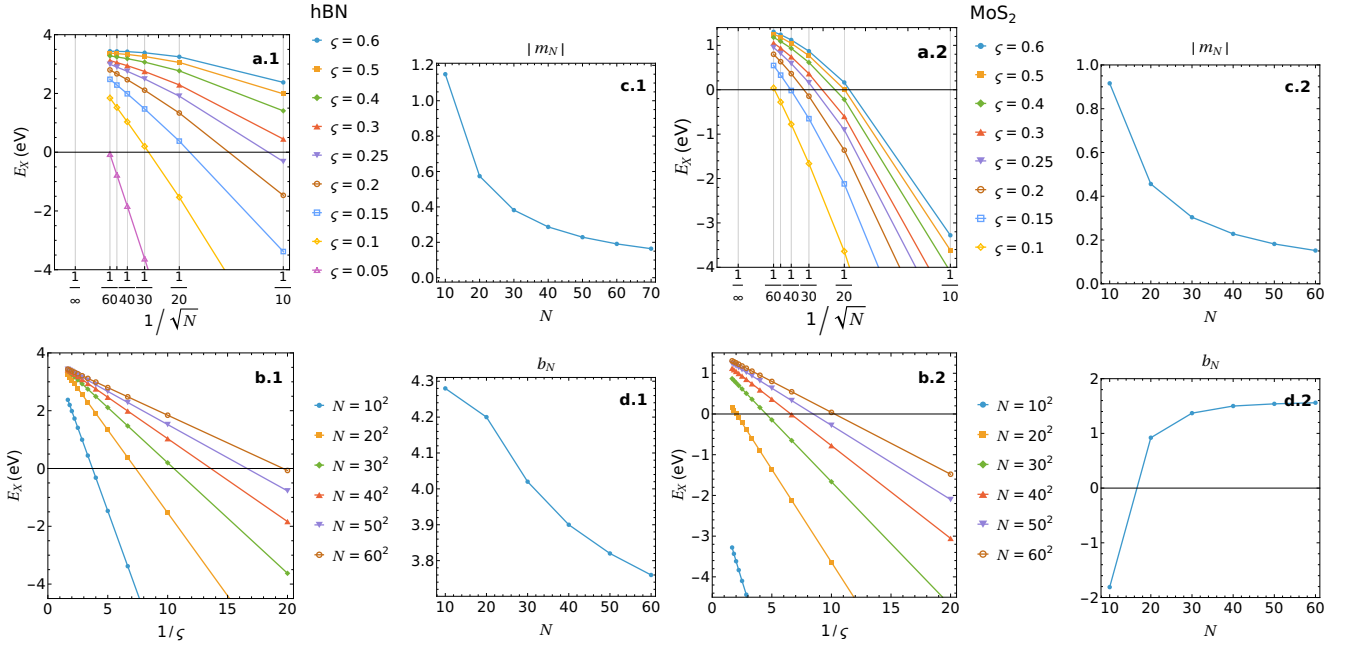


FIG. 5. **Convergence of the excitonic binding energy with the BZ mesh size and regularization radius.** Panels **a1-d1** present the results pertaining to hBN, while panels **a2-d2** pertain to MoS<sub>2</sub>. Panels **a1** and **a2** show the ground state excitonic energy level  $E_X$  as a function of  $N$  for different realizations of  $\zeta$ , which defines the radius of the regularization region as  $q_0 = \zeta k_0$ ,  $k_0$  being the length of the momentum vector closest to the origin in the BZ. Panels **b1** and **b2** show the dependence of  $E_x$  on  $\zeta^{-1}$  for different realizations of  $N$ , which follows a linear model as  $E_X = m_N \zeta^{-1} + b_N$ . The plot in panels **c1** and **c2** shows the behavior of the slope  $m_N$  with  $N$ , whereas panels **d1** and **d2** plot the origin off-set  $b_N$  versus  $N$ .

FIG. 6. **Convergence of the exciton binding energy with the cutoff.** These tables examine the convergence of the ground state excitonic binding energy, for hBN on the left and for MoS<sub>2</sub> on the right, with the cutoff  $G_c^e$  for the dielectric matrix, and with the cutoff  $G_c^X$  for the interaction matrix elements (always with  $G_c^X < G_c^e$ ). We have used  $N = 60^2$ ,  $N_c = N_v = 1$ , and we have excluded the exchange interaction term in both cases. For the size of the regularization region, we used the radius  $q_0 = \zeta k_0$ , where  $k_0$  is the norm of the wavevector(s) closest to the origin. We chose  $\zeta = 0.6$  for both materials. To obtain the binding energies in eV, we used for the electronic bandgap of hBN  $\Delta = 6.08$  eV, and for the bandgap of MoS<sub>2</sub> we used  $\Delta = 2.08$  eV, both values extracted from the band structure of these materials in Fig. 1. The entries in each table with  $> \Delta$  are entries for which we have obtained a binding energy higher than the electronic bandgap. As this is not physical, we just omit the values obtained.

		$G_c^e$ ( $\text{\AA}^{-1}$ )					
		0	3	5.1	6	8	9
$G_c^X$	0		4.209	5.617	5.814	6.071	$> \Delta$
	3		2.563	4.440	3.863	3.872	4.386
	5.1			2.857	3.054	3.948	4.690
	6				2.894	3.542	4.391
	8					2.961	5.872
	9						3.078

		$G_c^e$ ( $\text{\AA}^{-1}$ )					
		0	3	4	5	7	8
$G_c^X$	0		0.980	1.568	1.401	1.952	$> \Delta$
	3		0.756	1.619	1.786	$> \Delta$	$> \Delta$
	4			0.775	1.106	$> \Delta$	$> \Delta$
	5				0.778	$> \Delta$	$> \Delta$
	7					0.792	1.301
	8						0.799

quantum mechanical methods, the interacting problem is treated having one-particle non-interacting states as the working basis. Whence, before attacking the many-body problem, one has first to obtain a basis of eigenstates and eigenenergies by diagonalizing the Hamiltonian without interactions, or with interactions but at the mean-field level. In infinite periodic systems and small finite systems, the most widely used framework in the literature is the one provided by DFT. Through a

self-consistent formalism, the so-called Kohn-Sham (KS) method [5, 53, 54], one can obtain for a given material the set of quasiparticle energies  $\epsilon_n^{\text{KS}}$  that accurately describe its electronic structure. For infinite periodic systems, the most common ones in the field of solid state physics, momentum is a good quantum number and the electronic structure of the material is encoded in the dependence  $\epsilon_n^{\text{KS}}(\mathbf{k}) \equiv \epsilon_{n\mathbf{k}}$ . These quasiparticle energies compose the material band structure, just as represented in Fig. 1 for

hBN and MoS<sub>2</sub>, the materials under consideration in this work. In the early days of DFT, the electron–electron exchange and correlation contribution to the energy of the system was modeled within the LDA for the exchange–correlation functional. The LDA picture is well-known for underestimating the true electronic bandgap of semiconductors and insulators; this is the fundamental gap problem. To correctly estimate the bandgap of semiconductors and insulators, one can perform *GW* calculations as a post-processing step [22]. However, these involve the evaluation of the dielectric function beyond the static limit, which can be very heavy numerically.

As an alternative, one can introduce hybrid functionals to better model exchange–correlation effects. Hybrid functionals mix the exact Hartree–Fock (HF) functional, which is almost purely numerical, with an approximated one, say at the LDA or at the generalized gradient approximation (GGA) level [53, 54]. Generically, the hybrid functionals permit to better estimate the electronic bandgap than non-hybrid ones when compared with the experimental values [55], and at a much lower computational cost than *GW* methods. In this work, we bypass computationally intensive *GW* calculations by using the hybrid functional HSE06 [35], which mixes the exact HF exchange functional and the Perdew–Burke–Ernzerhof functional [56] within GGA. The calculations were done in a basis of localized Gaussian orbitals with the CRYSTAL code [34], as explained in Section II A. This package allows for obtaining a model Hamiltonian in a basis of localized orbitals, which is essential for us to apply the point-like orbital approximation. First mentioned in Section II B, this approximation shall be technically explained in the next section. The Hamiltonian obtained for each material serves then as a basis for describing the excitonic problem within an interacting picture beyond the mean-field level. The screening calculations necessary for the excitonic problem are performed on top of the same basis and are explained in the following subsections. Finally, the dielectric screening problem is followed by the calculation of the Bethe–Salpeter Hamiltonian and its diagonalization.

## B. Dielectric properties: polarizability and dielectric function

### 1. Polarizability

The non-interacting irreducible polarizability in momentum–frequency space reads [5, 51]

$$\chi_{\mathbf{G}\mathbf{G}'}^0(\mathbf{q}; \omega) = \frac{1}{N} \sum_{nn', \mathbf{k}\sigma} \frac{f_{n\mathbf{k}} - f_{n'\mathbf{k}+\mathbf{q}}}{\epsilon_{n\mathbf{k}} - \epsilon_{n'\mathbf{k}+\mathbf{q}} + \hbar\omega + i\hbar\alpha} \times \langle n, \mathbf{k} | e^{-i(\mathbf{q}+\mathbf{G})\cdot\mathbf{r}} | n', \mathbf{k} + \mathbf{q} \rangle \langle n', \mathbf{k} + \mathbf{q} | e^{i(\mathbf{q}+\mathbf{G}')\cdot\mathbf{r}} | n, \mathbf{k} \rangle, \quad (5)$$

where  $|n, \mathbf{k}\rangle$  represents a single-particle Bloch state of an electron (or hole) in the band  $n$  with momentum  $\mathbf{k}$ , and  $f_{n\mathbf{k}}$  is the occupation factor of the same state, the volume (area actually) of the crystal is given by  $N\Omega_{\text{UC}}$ , with  $\Omega_{\text{UC}}$  being the volume of the unit cell, and  $\alpha \rightarrow 0$  is an infinitesimal positive parameter.

The plane-wave matrix elements of the type  $\langle n, \mathbf{k} | e^{-i(\mathbf{k}'-\mathbf{k}+\mathbf{G})\cdot\mathbf{r}} | n', \mathbf{k}' \rangle \equiv I_{n\mathbf{k}, n'\mathbf{k}'}^{\mathbf{G}}$  are evaluated along the 2D material, ignoring the off-plane dimension so that the position vector  $\mathbf{r}$  is strictly in-plane. Within the linear combination of atomic orbitals (LCAO) and tight-binding (TB) approximations, the wavefunctions  $\psi_{n\mathbf{k}}(\mathbf{r}) = \langle \mathbf{r} | n, \mathbf{k} \rangle$  of the Bloch states, in the lattice gauge, are written in terms of localized orbitals  $\phi_{\alpha}$  as

$$\psi_{n\mathbf{k}}(\mathbf{r}) = \frac{1}{\sqrt{N}} \sum_{\mathbf{R}} e^{i\mathbf{k}\cdot\mathbf{R}} \sum_{i\alpha} C_{i\alpha}^{n\mathbf{k}} \phi_{\alpha}(\mathbf{r} - \mathbf{R} - \mathbf{t}_i), \quad (6)$$

with the sum in  $\mathbf{R}$  being over (all  $N$ ) unit cells of the Bravais lattice, and  $\mathbf{t}_i$  designates the position of the  $i$ th atom within the unit cell. The coefficients  $C_{i\alpha}^{n\mathbf{k}} = (\mathbf{C}^{n\mathbf{k}})_{i\alpha}$  are commonly called the TB coefficients, and they form the eigenvectors  $\mathbf{C}^{n\mathbf{k}}$  of the Bloch Hamiltonian, in the lattice gauge defined by  $H(\mathbf{k}) = \sum_{\mathbf{R}} \exp(i\mathbf{k}\cdot\mathbf{R})H(\mathbf{R})$ , where the Fock matrices  $H(\mathbf{R})$  are obtained from a Wannier interpolation (or from DFT calculations using a basis of localized functions, such as CRYSTAL [34]). This interpolation is performed after obtaining the quasiparticle band structure  $\{\epsilon_{n\mathbf{k}}\}$  through DFT calculations using a basis of delocalized functions (plane waves, for instance). Mathematically, in a basis where the orbitals are orthogonal, we write  $H(\mathbf{k})\mathbf{C}^{n\mathbf{k}} = \epsilon_{n\mathbf{k}}\mathbf{C}^{n\mathbf{k}}$ .

In equilibrium, the occupation factor  $f_{n\mathbf{k}}$  follows simply the Fermi–Dirac distribution, which in the zero absolute temperature limit is just a step function. It means that for an energy below the Fermi energy  $f_{n\mathbf{k}} = 1$ , and zero otherwise. In this paper we discuss only intrinsic semiconductors and insulators, that at zero temperature have all the bands below the Fermi energy completely filled, and those above the Fermi energy are empty. The ground state is that of all the valence bands filled and the conduction bands empty, with a gap of forbidden energies separating them. In the static limit  $\omega \rightarrow 0$  and at zero temperature, and if time-reversal symmetry (TRS) is present, the expression (5) above reduces to expression (1). We refer to Section S1 of the SI for a detailed proof. The matrix elements in the numerator can be computed by evaluating the real-space integral

$$I_{n\mathbf{k}, n'\mathbf{k}'}^{\mathbf{G}} = \int_{\Omega} \psi_{n\mathbf{k}}^*(\mathbf{r}) e^{-i(\mathbf{k}'-\mathbf{k}+\mathbf{G})\cdot\mathbf{r}} \psi_{n'\mathbf{k}'}(\mathbf{r}) d\mathbf{r} = \sum_{i\alpha} (C_{i\alpha}^{n\mathbf{k}})^* C_{i\alpha}^{n'\mathbf{k}'} e^{-i(\mathbf{k}'-\mathbf{k}+\mathbf{G})\cdot\mathbf{t}_i} \quad (7)$$

taken over the entire crystal, and where the last equality was obtained after replacing the Bloch state wavefunctions  $\psi_{n\mathbf{k}}(\mathbf{r})$  by their respective LCAO expansion

as per (6) and simplifying. We also used the identity  $\phi_\alpha(\mathbf{r}-\mathbf{R}-\mathbf{t}_i)\phi_\beta(\mathbf{r}-\mathbf{R}'-\mathbf{t}_j) \approx \delta_{\alpha\beta}\delta_{\mathbf{R}\mathbf{R}'}\delta_{ij}\delta(\mathbf{r}-\mathbf{R}-\mathbf{t}_i)$ , the so called point-like orbital approximation within which the orbitals are extremely localized around the atomic positions [28]. We make here a pertinent technical remark. These orbitals at hand might not necessarily be atomic orbitals in a TB description of the Hamiltonian, but they may also be interpreted as Wannier orbitals [32] of a Hamiltonian obtained from the Wannier interpolation of the DFT bands. So, instead of seeing these orbitals as several atomic orbitals localized at each position  $\mathbf{t}_i$  of the  $i$ th atom in the motif of the unit cell, we can see them as a set of Wannier orbitals, each one localized at a Wannier center that in general does not coincide with atomic sites in the lattice. Then,  $\mathbf{t}_i$  is no longer a position of an atom in the motif, but the  $i$ th Wannier center within the unit cell.

We have tested our implementation with Wannier models as well and with good results, in particular for MoS<sub>2</sub>, something discussed in more detail in Section S4 of the SI. During our investigations, we observed that the head element of the polarizability for an isotropic material when plotted as a function of  $q = |\mathbf{q}|$  with  $\mathbf{q}$  covering the whole BZ, like in Fig. 3, may present considerable numerical fluctuations. Instead, one should obtain a dependence on  $q$  presenting a single curve as expected for isotropic materials. Those models, with the band structure calculated through DFT followed by a Wannier interpolation using the WANNIER90 code, were obtained without forcing the symmetry preservation when running WANNIER90. Therefore, the symmetries of a material model Hamiltonian may play a role in its dielectric properties, most likely those related to the space group of the crystalline material, which can be violated when performing a faulty Wannier interpolation. However, the exact role that space group symmetries play in the polarizability is unclear to us.

The irreducible polarizability  $\chi^{\text{irr}}$  and the full interacting one  $\chi$  are connected through Dyson equation  $\chi = \chi^{\text{irr}} + \chi^{\text{irr}}V\chi$  [20, 22], where  $V$  is the Coulomb interaction kernel, and in general includes the direct unscreened Coulomb interaction  $v_c(\mathbf{r} - \mathbf{r}') = e/4\pi\epsilon_0|\mathbf{r} - \mathbf{r}'|$  and exchange-correlation terms, with the last being discarded in this work. Exchange terms are also ignored in the irreducible polarizability, leading to its non-interacting limit  $\chi^{\text{irr}} \rightarrow \chi^0$ , where only the Hartree diagram is kept (leaving out the Fock terms). The random-phase approximation (RPA) counterpart of the full polarizability  $\chi \rightarrow \chi^{\text{RPA}}$  can therefore be obtained by solving the Dyson equation [20, 22]

$$\chi^{\text{RPA}} = \chi^0 + \chi^0V_c\chi^{\text{RPA}}, \quad (8)$$

where the Coulomb kernel  $V_c$  includes only the bare Coulomb potential. In momentum space, the previous equation is a matrix equation for each momentum  $\mathbf{q} \in \text{BZ}$ , with the Coulomb kernel having matrix elements

$(V_c)_{\mathbf{G}\mathbf{G}'} = v_c(\mathbf{q} + \mathbf{G})\delta_{\mathbf{G}\mathbf{G}'}$ , where the expression for the Fourier transformed Coulomb potential depends on the number of dimensions. Typically, *ab initio* calculations include exchange-correlation contributions to the Coulomb kernel [22, 37, 38], and eventually other terms accounting for relativistic effects such as spin, but doing so is beyond the scope of this work. Furthermore, *ab initio* calculations are done in 3D (using off-plane periodic images for 2D materials), whence the commonly used momentum-resolved Coulomb potential in the literature is the 3D one, for which

$$v_c(\mathbf{q}) = \frac{e}{\epsilon_0|\mathbf{q}|^2\Omega_{\text{UC}}}, \quad (9)$$

with  $\Omega_{\text{UC}}$  denoting the volume of the unit cell. However, in this work we operate strictly within a 2D framework, as information about the system in the  $z$  direction is either inaccessible or deliberately disregarded. Consequently, we use the 2D Fourier-transformed potential. This is commonly done and has shown to produce good results, both in analytical calculations for the dielectric function in atomically thin materials, such as the semimetal graphene [57, 58], and for excitons [14, 28–30, 36, 38, 59–61] in 2D semiconductors and insulators. To the best of our knowledge, a fully numerical and 2D treatment of the dielectric function has not been done. This is the topic of the next subsection.

## 2. Direct and inverse dielectric function

In the manner described above, the inverse RPA dielectric function can be obtained through the definition

$$\epsilon_{\mathbf{G}\mathbf{G}'}^{-1}(\mathbf{q}) = \delta_{\mathbf{G}\mathbf{G}'} + \chi_{\mathbf{G}\mathbf{G}'}^{\text{RPA}}(\mathbf{q})v_c(\mathbf{q} + \mathbf{G}'). \quad (10)$$

Alternatively, the same quantity can be obtained by computing the dielectric function matrix directly, which within RPA is given by

$$\epsilon_{\mathbf{G}\mathbf{G}'}(\mathbf{q}) = \delta_{\mathbf{G}\mathbf{G}'} - v_c(\mathbf{q} + \mathbf{G})\chi_{\mathbf{G}\mathbf{G}'}^0(\mathbf{q}), \quad (11)$$

and subsequently inverting it. In this work, we adopt the latter approach, though we still consider the former worth mentioning.

The 2D version of the implementation of the dielectric function has a striking advantage compared to the 3D counterpart when it comes to numerical instabilities, namely when computing the dielectric matrix around the origin  $\mathbf{q} \sim 0$  and exactly at the origin, when  $\mathbf{q} = 0$ . For very small momentum transfer, the polarizability scales as  $q^2$  for 2D semiconductors and insulators [37], a behavior we have already verified in Subsection II B. As a result,  $v_c(q)\chi_{00}^0(q) \sim \mathcal{O}(q)$  as  $q \rightarrow 0$ , which ensures that no numerical instability arises at the origin for the head matrix element of the dielectric function,

$\varepsilon_{\mathbf{00}}(\mathbf{0})$ . In this way, we can avoid having to use numerical schemes just to treat the problem of computing directly this matrix element, unlike other implementations in the literature, for instance the BerkelyGW one from Deslippe *et al.* [37]. For this particular matrix element, it does not matter whether one implements the dielectric function as per Eq. (11), or its symmetrized version  $\varepsilon_{\mathbf{G}\mathbf{G}'}(\mathbf{q}) \rightarrow \varepsilon_{\mathbf{G}\mathbf{G}'}(\mathbf{q})\sqrt{v_c(\mathbf{q}+\mathbf{G}')}/\sqrt{v_c(\mathbf{q}+\mathbf{G})}$  as per Eq. (2). But as we will see, to deal with the wing elements  $\varepsilon_{\mathbf{G}\mathbf{0}}(\mathbf{0})$  and  $\varepsilon_{\mathbf{0}\mathbf{G}}(\mathbf{0})$  it is more convenient—both technically and computationally—to use the symmetrized form of the dielectric function [62–64]. Whence, we have chosen to implement the expression (2) instead of expression (11). Exactly at the origin, there is general consensus in the literature that some form of regularization must be applied to the dielectric matrix. Naturally, the screened potential also requires regularization, although we defer that discussion to Section III C. The regularization is essential to prevent divergences or undefined values in the matrix elements of the inverse dielectric function—and consequently in the screened potential—ensuring that subsequent calculations, such as determining excitonic energies and wavefunctions, are not compromised by numerical errors.

Based on the discussion above, one can immediately conclude that the head matrix element satisfies  $\varepsilon_{\mathbf{00}}(\mathbf{0}) = 1$ . For the wing elements of the inverse dielectric matrix of both forms  $\varepsilon_{\mathbf{G}\mathbf{0}}^{-1}(\mathbf{q})$  and  $\varepsilon_{\mathbf{0}\mathbf{G}}^{-1}(\mathbf{q})$ , if the symmetrized dielectric function is adopted, they approach zero when  $q \rightarrow 0$  with  $\sim \sqrt{q}$  (see Section S2 of the SI). In practical implementations, it is therefore reasonable to set  $\varepsilon_{\mathbf{G}\mathbf{0}}^{-1}(\mathbf{0}) = \varepsilon_{\mathbf{0}\mathbf{G}}^{-1}(\mathbf{0}) = 0$ . Nevertheless, it remains important to understand the precise behavior of this limit in order to correctly regularize the screened potential—a topic addressed in the following section.

Our implementation allows for making a plausible estimate of the static macroscopic dielectric function of 2D materials with reasonable computational effort, through the commonly adopted definition in the literature [40]

$$\varepsilon_M(\mathbf{q}) \equiv \frac{1}{\varepsilon_{\mathbf{00}}^{-1}(\mathbf{q})} \neq \varepsilon_{\mathbf{00}}(\mathbf{q}), \quad (12)$$

stressing that it does not coincide with the head matrix element of the dielectric function due to the local-field effects [51, 52][65]. This is confirmed with the analysis of the inverse dielectric matrix in Section S2 of the SI. We have actually verified numerically, but do not show here, that ignoring the local-field effects overestimates the screening by far, unless the momentum transfer is very small, for which  $\varepsilon_{\mathbf{00}}(\mathbf{q}) \approx 1/\varepsilon_{\mathbf{00}}^{-1}(\mathbf{q})$ . Notably, this definition remains valid beyond the static regime. However, computing the dielectric function as a function of frequency lies beyond the scope and purpose of this manuscript.

It is more than pertinent to stress here a key point in our work. Due to the 2D nature of our calculations,

the previously defined macroscopic dielectric function is actually the 2D effective macroscopic dielectric function. This is not true in general in *ab initio* calculations, where the calculations are in 3D, and the results for 2D systems have to be converged against the amount of vacuum between adjacent repeated images,  $L_\perp$ . In *ab initio* calculations, the bare Coulomb potential used in practice for 2D materials is a truncated one and not Eq. (9), serving the purpose of speeding up the convergence by diminishing the Coulomb interaction between consecutive repeated system images. It carries no physical meaning, and simply constitutes a numerical trick. Nonetheless, the calculations always have to be converged with  $L_\perp$ . To argument in favor of our calculations, a truncation of the Coulomb potential in real space is deemed unnecessary, as we work directly with its 2D Fourier transform. Furthermore, the macroscopic dielectric function defined by Eq. (12) is always one at zero momentum, and by consequence the head element of the inverse dielectric matrix is unity too. This is so by virtue of the polarizability reaching zero quadratically in momentum when the momentum approaches zero, but the Coulomb potential diverges with  $1/q$ . In sharp contrast, in *ab initio* calculations the macroscopic in-plane dielectric function at zero momentum is unity only in the limit of infinite  $L_\perp$  [41]. Moreover, the definition (12) for 3D systems is valid only if we interpret that macroscopic dielectric function as a bulk one, while for 2D systems some sort of off-plane average has to be performed to obtain the true effective 2D macroscopic dielectric function [24, 25, 40].

Based on the analysis of our numerical macroscopic dielectric function in Section II C, we conclude that our strictly 2D computation of the microscopic dielectric function—followed by its inversion—naturally yields a macroscopic dielectric response that is inherently 2D. In contrast to 3D first-principles methods, our approach avoids off-plane image contributions entirely, eliminating the need for any off-plane averaging to define an effective 2D dielectric function. The macroscopic response emerges directly and unambiguously from our 2D framework. The trade-off is that with a strict 2D approach, one cannot capture correctly the dielectric function beyond the small- $q$  limit. To improve the accuracy of the dielectric properties of 2D systems using a 2D framework for the dielectric function, we can take the off-plane distances within the monolayer into account through a mixed representation for screening, mixing the momentum dependence of the dielectric function with the real-space dependence. That is the subject of the next section.

### 3. Quasi-2D approach for the dielectric function

In this section we discuss the quasi-two-dimensional (Q2D) approach for the dielectric function adopted in this manuscript. It allows for incorporating the electronic

structure pertaining to the off-plane physics. While the system is infinite (and periodic) along the  $x$  and  $y$  directions, which permits the electrons in Bloch states to propagate along the crystal, the electrons are confined along the  $z$  direction.

Unlike in *ab initio* approaches, where the system is periodic in all three Cartesian axis, herein the momentum is not a good quantum number for describing the delocalization of the electrons along the material thickness. Therefore, we are not allowed to perform a full 3D Fourier transform on the real-space (RPA) dielectric function given by

$$\varepsilon(\mathbf{r}, \mathbf{r}') = \delta(\mathbf{r} - \mathbf{r}') - \int v_c(\mathbf{r} - \mathbf{x}) \chi^0(\mathbf{x}, \mathbf{r}') d\mathbf{x}, \quad (13)$$

where, for simplicity, we have omitted the dynamic nature of the dielectric function. Regardless of the dimensionality (that is, the number of dimensions along which the material is infinite) of the system, the real-space integral is over a volume region; the atomic orbitals of the individual atoms in the crystal have a 3D spatial structure, and the same can be said about the electron density  $n(\mathbf{r})$ .

In 3D systems, it is possible to work with a dielectric function defined in the 3D reciprocal space. The identity (11) still holds, but both the momentum  $\mathbf{q}$  and reciprocal lattice vectors  $\mathbf{G}$  and  $\mathbf{G}'$  are 3D, having a  $z$  component in reciprocal space. Also, the bare Coulomb potential follows Eq. (9). This is the approach commonly found in the literature on computational methods for dielectric screening.

In our formalism, a 3D Fourier transform of Eq. (13) is not useful. Instead, we perform a partial 2D Fourier transform of the real-space-resolved dielectric function, and keep track of the spatial  $z$ -dependence at the same time. Then, we work with the dielectric function in a mixed representation that reads

$$\varepsilon_{\mathbf{G}\mathbf{G}'}(\mathbf{q}, z, z') = \delta_{\mathbf{G}\mathbf{G}'} \delta(z - z') - \frac{e}{2\varepsilon_0 |\mathbf{q} + \mathbf{G}| \Omega_{UC}} \int_{-\infty}^{\infty} dz'' e^{-|\mathbf{q} + \mathbf{G}| |z - z''|} \chi_{\mathbf{G}\mathbf{G}'}^0(\mathbf{q}, z'', z'), \quad (14)$$

where both (in-plane) momentum and  $z$  variables are present, the vectors  $\mathbf{G}$  and  $\mathbf{G}'$  are vectors of the recipro-

cal lattice, which is 2D, the polarizability  $\chi_{\mathbf{G}\mathbf{G}'}^0(\mathbf{q}, z, z')$  appears also in the mixed representation and is convoluted in the  $z$  variable with the bare Coulomb potential in the mixed representation given by

$$v_c(\mathbf{q}, z - z') = \frac{e}{2\varepsilon_0 q} e^{-q|z - z'|}. \quad (15)$$

The previous expression for the Coulomb potential is the main ingredient in our Q2D formalism. It is not hard to show that the previous expression is the Fourier transform of the position-resolved Coulomb potential along the  $xy$  plane in real space. In the limit  $z = z'$ , we recover the strict 2D Fourier transform of the Coulomb potential.

The polarizability in the mixed representation, which we will call the  $(\mathbf{q}, z)$ -representation from now on, is defined as the 2D Fourier transform of the real-space-resolved polarizability  $\chi^0(\mathbf{r}, \mathbf{r}')$ , where the in-plane spatial integrals are over the entire crystal (that is finite, and using periodic boundary conditions). To have a discussion as self-contained as possible, we provide the general expression for the non-interacting, irreducible RPA polarizability in real space. If we also want to include the frequency dependence of the polarizability, then we can write [5]

$$\chi^0(\mathbf{r}, \mathbf{r}'; \omega) = \sum_{i,j} (f_i - f_j) \frac{\phi_i^*(\mathbf{r}) \phi_j(\mathbf{r}) \phi_j^*(\mathbf{r}') \phi_i(\mathbf{r}')}{\varepsilon_i - \varepsilon_j + \hbar\omega + i\eta}, \quad (16)$$

where  $\eta$  is a small infinitesimal parameter,  $i$  and  $j$  represent a set of quantum numbers,  $\phi_i(\mathbf{r})$  is the  $i$ -th state with eigenenergy  $\varepsilon_i$ , and  $f_i$  is the Fermi-Dirac distribution [66] computed at the energy  $\varepsilon_i$ . The states  $\phi_i(\mathbf{r})$  are obtained within a mean-field approach, such as within HF theory or the Kohn-Sham framework of DFT. In our work-flow, the band structure calculations are done prior to the screening calculations to obtain the model Hamiltonian for the material at hand. Then, we identify the states  $\phi_i(\mathbf{r})$  with the Bloch states  $\psi_{n\mathbf{k}}(\mathbf{r})$  in the LCAO approximation as per (6), and the quasi-particle energies  $\varepsilon_i$  with  $\varepsilon_{n\mathbf{k}}$ .

In this article, we consider zero absolute temperature (or a low enough temperature such that conduction states in a semiconductor remain unpopulated), and work in the static limit  $\omega \rightarrow 0$  (which also allows to set  $\eta = 0$ ). This simplifies our calculations. By performing an in-plane Fourier transform on (16) in these approximations and applying the point-like orbital approximation, we obtain

$$\begin{aligned} \chi_{\mathbf{G}\mathbf{G}'}^0(\mathbf{q}, z, z') &= \frac{1}{N} \sum_{vc, \mathbf{k}\sigma} \frac{1}{(\epsilon_{v\mathbf{k}} - \epsilon_{c\mathbf{k}+\mathbf{q}})} \\ &\left\{ \sum_{i\alpha} \left[ C_{i\alpha}^{c\mathbf{k}+\mathbf{q}} (C_{i\alpha}^{v\mathbf{k}})^* e^{-i(\mathbf{q}+\mathbf{G})\cdot\mathbf{t}_i} \delta(z - t_{i,z}) \right] \sum_{j\beta} \left[ C_{j\beta}^{v\mathbf{k}} (C_{j\beta}^{c\mathbf{k}+\mathbf{q}})^* e^{i(\mathbf{q}+\mathbf{G}')\cdot\mathbf{t}_j} \delta(z' - t_{j,z}) \right] + \right. \\ &\left. \sum_{i\alpha} \left[ (C_{i\alpha}^{c\mathbf{k}+\mathbf{q}})^* C_{i\alpha}^{v\mathbf{k}} e^{-i(\mathbf{q}+\mathbf{G})\cdot\mathbf{t}_i} \delta(z - t_{i,z}) \right] \sum_{j\beta} \left[ (C_{j\beta}^{v\mathbf{k}})^* C_{j\beta}^{c\mathbf{k}+\mathbf{q}} e^{i(\mathbf{q}+\mathbf{G}')\cdot\mathbf{t}_j} \delta(z' - t_{j,z}) \right] \right\}. \quad (17) \end{aligned}$$

To obtain this result, one has to separate the  $\mathbf{r}_{\parallel}$  and  $z$  variables when doing the point-like orbital approximation as  $\delta(\mathbf{r} - \mathbf{R} - \mathbf{t}_i) = \delta(\mathbf{r}_{\parallel} - \mathbf{R} - \mathbf{t}_{i,\parallel})\delta(z - t_{i,z})$ , and in analogy we do the same for the primed variables  $\mathbf{r}'_{\parallel}$  and  $z'$ . This expression for the polarizability in the  $(\mathbf{q}, z)$ -representation is the one we use in Eq. (14) for the dielectric function. In this way, we are able to take into account the finite thickness of the material, that we will denote by  $d_{\perp}$ , and the out-of-plane position  $t_{i,z}$  of the atoms composing the unit cell motif. By averaging the dielectric function over the monolayer thickness, we can define an effective Q2D microscopic dielectric function as

$$\bar{\epsilon}_{\mathbf{G}\mathbf{G}'}(\mathbf{q}) \equiv \frac{1}{d_{\perp}} \int_{-d_{\perp}/2}^{d_{\perp}/2} \int_{-d_{\perp}/2}^{d_{\perp}/2} \epsilon_{\mathbf{G}\mathbf{G}'}(\mathbf{q}, z, z') dz dz', \quad (18)$$

where the integrals can be performed exactly by virtue of the properties of the Dirac delta-function. As dictated by the definition (12), we can define an effective Q2D macroscopic dielectric function as  $\epsilon_M(\mathbf{q}) = (\bar{\epsilon}_{\mathbf{0}\mathbf{0}}^{-1}(\mathbf{q}))^{-1}$ . Using this new definition for the macroscopic dielectric function was how we obtained the results in Fig. 4.

Solely by analytical calculations, we can show that the averaged Q2D dielectric function of Eq. (18) coincides with its strict 2D counterpart from Eq. (2) in the zero thickness limit. Using maths notation, we can write

$$\epsilon_{\mathbf{G}\mathbf{G}'}(\mathbf{q}) = \lim_{d_{\perp} \rightarrow 0} \bar{\epsilon}_{\mathbf{G}\mathbf{G}'}(\mathbf{q}). \quad (19)$$

This result allows us to define the long-wavelength or low- $q$  limit as the values of  $q$  for which  $qd_{\perp} \ll 1$ . Furthermore, it explains why in this limit the 2D, Q2D and *ab initio* macroscopic dielectric functions agree with each other. The Q2D dielectric function was not used to compute the excitons, but we did so with the 2D one. More specifically, the matrix elements of the 2D inverse dielectric function were used to compute the interaction matrix elements that enter in the BSE, the subject of the next section.

### C. Bethe–Salpeter equation

Excitons in semiconductors and insulators play a crucial role in determining their optical properties, particularly in the frequency range corresponding to sub-gap energies. These excitonic effects can only be accurately described by accounting for electron–electron and electron–hole interactions beyond the mean-field level. Such interactions are mediated by the Coulomb potential, which, in a crystalline material, is screened due to charge polarization. This screening is quantified by the dielectric function we have been analyzing throughout this work. Due to the Coulomb attraction between the electron and the hole, they can form a bound excitonic state  $|X\rangle$  with an energy  $E_X$  lying within the bandgap of the material. We assume that the excitonic state can be expressed as a linear combination of unbound electron–hole pair states, where the electron occupies a single-particle state in a conduction band  $c$  and the hole corresponds to an absence of an electron in a valence band  $v$ . Formally,  $|X\rangle = \sum_{\mathbf{k}, v, c} A_{vc}(\mathbf{k}) c_{c, \mathbf{k}}^{\dagger} c_{v, \mathbf{k}} |\text{FS}\rangle$ , where the sum runs over pairs of valence and conduction bands, and only vertical transitions (same  $\mathbf{k}$ ) are considered. Here,  $|\text{FS}\rangle$  denotes the ground state of the semiconductor or insulator (the Fermi sea). The exciton energy  $E_X$  can be determined by solving the BSE, which, within the Tamm–Dancoff approximation, reads [67]:

$$\begin{aligned} (\epsilon_{c\mathbf{k}} - \epsilon_{v\mathbf{k}}) A_{vc}(\mathbf{k}) \\ + \sum_{c', v', \mathbf{k}'} K_{vc, v'c'}(\mathbf{k}, \mathbf{k}') A_{v'c'}(\mathbf{k}') = E_X A_{vc}(\mathbf{k}). \quad (20) \end{aligned}$$

Here, the first term on the left-hand side (LHS) accounts for the vertical transition between single-particle states and the second one, accounting for the electron–hole interaction, is quantified by matrix elements of the many-body interaction kernel  $K = -(D - X)$ , that includes a direct term  $D$  and an exchange term  $X$ . For instance, the direct term writes

$$\begin{aligned} D_{vc, v'c'}(\mathbf{k}, \mathbf{k}') \\ = \int d\mathbf{r} d\mathbf{r}' \psi_{c\mathbf{k}}^*(\mathbf{r}) \psi_{v\mathbf{k}'}^*(\mathbf{r}') W(\mathbf{r}, \mathbf{r}') \psi_{c'\mathbf{k}'}(\mathbf{r}) \psi_{v'\mathbf{k}}(\mathbf{r}') \quad (21) \end{aligned}$$

in the approximation of static screening. The exchange term is obtained by simply exchanging  $c', \mathbf{k}'$  with  $v, \mathbf{k}$ . Unlike the BSE derived from MBPT, where the exchange term is typically treated as unscreened, our approach does not require the exchange term to be unscreened, as justified in Ref. 28.

We model the static screened potential through the dielectric function in momentum space that we have computed previously. The relation between the screened Coulomb potential and the bare one is established through a Dyson equation, analogous to Eq. (8), that within RPA writes [5]

$$W = V_c + V_c \chi^0 W. \quad (22)$$

Upon solving for  $V_c$  in terms of  $W$ , defining  $\varepsilon = \mathbb{1} - V_c \chi^0$  and inverting the relation, in momentum space we can write

$$W_{\mathbf{G}\mathbf{G}'}(\mathbf{q}) = \varepsilon_{\mathbf{G}\mathbf{G}'}^{-1}(\mathbf{q}) v_c(\mathbf{q} + \mathbf{G}'). \quad (23)$$

Here,  $\varepsilon_{\mathbf{G}\mathbf{G}'}^{-1}(\mathbf{q})$  is the  $(\mathbf{G}\mathbf{G}')$  matrix element of the inverse of the dielectric matrix as per (11), at the point  $\mathbf{q}$  in the BZ. We implement the symmetrized dielectric matrix; therefore, the correct relation is  $W_{\mathbf{G}\mathbf{G}'}(\mathbf{q}) = \sqrt{v_c(\mathbf{q} + \mathbf{G})} \varepsilon_{\mathbf{G}\mathbf{G}'}^{-1}(\mathbf{q}) \sqrt{v_c(\mathbf{q} + \mathbf{G}')}$ . Given the matrix elements of the screened potential and the expansion of the Bloch states in a basis of localized orbitals as in Eq. (6), the direct matrix element in Eq. (21), within the point-like orbital approximation and after Fourier transforming and simplifying the screened potential, is given by

$$D_{v_c, v'_c}(\mathbf{k}, \mathbf{k}') = \frac{1}{N} \sum_{\mathbf{G}\mathbf{G}'} I_{c\mathbf{k}, c'\mathbf{k}'}^{\mathbf{G}} W_{\mathbf{G}\mathbf{G}'}(\mathbf{k} - \mathbf{k}') (I_{v\mathbf{k}, v'\mathbf{k}'}^{\mathbf{G}'})^*, \quad (24)$$

where each capital  $I$  is a plane-wave matrix element between Bloch states, just as we defined initially in Section II B, and are evaluated by using Eq. (7).

The exchange term takes a similar form, but we do not include it in the calculations (however, one must do so for non-vertical transitions where  $\mathbf{Q} \neq \mathbf{0}$ ).

It has previously been demonstrated that evaluating the screened potential in real space leads to significantly faster convergence of the calculations compared to evaluating it in momentum space [28]. Conversely, it has also been reported that explicitly including the  $\mathbf{q} = \mathbf{0}$  term improves the numerical convergence with respect to the number of  $\mathbf{k}$ -points used [63]. Here, we adopt a regularization scheme for the term  $W_{\mathbf{0}\mathbf{0}}(\mathbf{q} = \mathbf{0})$  proposed in Ref. 41, which we discuss in detail in Sec. S2 of the SI. To our knowledge, this approach has not been applied previously.

For the sake of making the main text as self-contained as possible, we explain how we regularized the potential for the singular terms when  $\mathbf{q} = \mathbf{0}$ . As proposed in Ref. 41, the head matrix element of the screened potential at the origin is replaced by an average, integrating

the screened potential in a sufficiently small region  $\Omega_\Gamma$  centered at the origin  $\Gamma$  of the BZ, that we take here as a small circle of radius  $q_0$ . The average reads

$$W_{\mathbf{0}\mathbf{0}}(\mathbf{0}) = \frac{1}{\Omega_\Gamma} \int_{\Omega_\Gamma} d\mathbf{q} v_c(\mathbf{q}) [1 + \mathbf{q} \cdot \nabla_{\mathbf{q}} \varepsilon_{\mathbf{0}\mathbf{0}}^{-1}(\mathbf{q})|_{\mathbf{q}=\mathbf{0}}], \quad (25)$$

and can be computed analytically by numerically evaluating the gradient appearing in the expression. We know that the head matrix element of the inverse dielectric function is linear in  $\mathbf{q}$  for  $\mathbf{q} \sim 0$ , so that  $\nabla_{\mathbf{q}} \varepsilon_{\mathbf{0}\mathbf{0}}^{-1}(\mathbf{q})|_{\mathbf{q}=\mathbf{0}} = (-r_0^x, -r_0^y)$ , where we use two screening parameters, one along the  $x$  direction and the other along the  $y$  direction (directions in reciprocal space, that is). Henceforth,  $r_0^x$  and  $r_0^y$  are estimated numerically to evaluate (25). If the material is isotropic, which is the case of both hBN and MoS<sub>2</sub>, then  $r_0^x = r_0^y$ , and only  $r_0^x$  needs to be computed.

The other matrix elements that require treatment by hand are the wing ones. However, we argue in Section S2 of the SI that these matrix elements can be simply ruled out and take them as null:  $W_{\mathbf{G}\mathbf{0}}(\mathbf{0}) = W_{\mathbf{0}\mathbf{G}}(\mathbf{0}) = 0$ . This is a byproduct, and another advantage, of the Coulomb potential in our implementation diverging with  $1/q$  instead of  $1/q^2$ . In this way, we avoid the need for performing numerical angular averages for these matrix elements as it is done in previous works [63]. Even though the low  $q$ -dependence, just as in Ref. 63, goes with the direction  $\hat{\mathbf{q}} = \mathbf{q}/q$  along which we take the limit, in our case it does so linearly (see equations (S.22) and (S.23) of the SI). Hence, performing a numerical average (over a centrosymmetric region to fully account for eventual anisotropies) would yield a null result.

## ACKNOWLEDGMENTS

We thank Nuno M. R. Peres for stimulating and insightful discussions. We thank Guilherme Janone for providing the Wannier model for MoS<sub>2</sub> and M. Quintela for testing the beta version of XATU. P. N. acknowledges support by the Otto Mønsted Foundation (grant No. 24-70-1631) and the Independent Research Fund Denmark (grant No. 2032-00045A). The Center for Polariton-driven Light-Matter Interactions (POLIMA) is funded by the Danish National Research Foundation (project No. DNRF165). J. J. P. acknowledges the Spanish Ministry of Science, Innovation and Universities and the State Research Agency (MCIU/AEI/FEDER,UE) through Grant No. PID2022-141712NB-C21, the ‘‘María de Maeztu’’ Programme for Units of Excellence in R&D (CEX2023-001316-M), the Comunidad de Madrid within the Recovery, Transformation and Resilience Plan, and by NextGenerationEU programme from the European Union through the project ‘‘Disruptive 2D materials’’ (MAD2D-CM-UAM7), the Generalitat Valenciana through the Program Prometeo (2021/017), and

the Naturgy Foundation. We also acknowledge computer resources and assistance provided by Centro de Computación Científica de la Universidad Autónoma de Madrid and RES resources (FI-2025-3-36, FI-2025-2-34, FI-2025-1-12, FI-2024-3-0010, FI-2024-2-0016, FI-2024-1-0038).

## AUTHOR CONTRIBUTIONS

P. N. designed and conducted the research; A. J. U.-A. developed the first version of the code, introduced the first author to it and gave advice on the implementation of the new functionalities; J. J. P. analyzed the data; C. T., N. A. M. and J. J. P. supervised the research; and P. N., A. J. U.-A., C. T., N. A. M. and J. J. P. wrote the manuscript.

- 
- [1] M. Fox, *Optical Properties of Solids*, 2nd ed., Oxford Master Series in Physics (Oxford University Press, Oxford, New York, 2010).
- [2] C. Kittel, *Introduction to Solid State Physics* (Wiley, 2004).
- [3] H. Haug and S. W. Koch, *Quantum Theory of the Optical and Electronic Properties of Semiconductors*, 5th ed. (World Scientific, 2009).
- [4] G. D. Mahan, *Many Particle Physics, Third Edition* (Plenum, New York, 2000).
- [5] M. L. Cohen and S. G. Louie, *Fundamentals of Condensed Matter Physics* (Cambridge University Press, 2016).
- [6] F. Ferreira, A. J. Chaves, N. M. R. Peres, and R. M. Ribeiro, Excitons in hexagonal boron nitride single-layer: a new platform for polaritonics in the ultraviolet, *Journal of the Optical Society of America B* **36**, 674 (2019).
- [7] C. Elias, P. Valvin, T. Pelini, A. Summerfield, C. J. Mellor, T. S. Cheng, L. Eaves, C. T. Foxon, P. H. Beton, S. V. Novikov, B. Gil, and G. Cassabois, Direct band-gap crossover in epitaxial monolayer boron nitride, *Nature Communications* **10**, 2639 (2019).
- [8] A. Ramasubramaniam, Large excitonic effects in monolayers of molybdenum and tungsten dichalcogenides, *Physical Review B* **86**, 115409 (2012).
- [9] T. C. Berkelbach, M. S. Hybertsen, and D. R. Reichman, Theory of neutral and charged excitons in monolayer transition metal dichalcogenides, *Physical Review B* **88**, 045318 (2013).
- [10] L. C. Flatten, Z. He, D. M. Coles, A. a. P. Trichet, A. W. Powell, R. A. Taylor, J. H. Warner, and J. M. Smith, Room-temperature exciton-polaritons with two-dimensional WS<sub>2</sub>, *Scientific Reports* **6**, 33134 (2016).
- [11] S. Morozov, C. Wolff, and N. A. Mortensen, Room-temperature low-voltage control of excitonic emission in transition metal dichalcogenide monolayers, *Advanced Optical Materials* **9**, 2101305 (2021).
- [12] J. Fang, K. Yao, M. Wang, Z. Yu, T. Zhang, T. Jiang, S. Huang, B. A. Korgel, M. Terrones, A. Alù, and Y. Zheng, Observation of room-temperature exciton-polariton emission from wide-ranging 2D semiconductors coupled with a broadband Mie resonator, *Nano Letters* **23**, 9803–9810 (2023).
- [13] A. Chernikov, T. C. Berkelbach, H. M. Hill, A. Rigosi, Y. Li, B. Aslan, D. R. Reichman, M. S. Hybertsen, and T. F. Heinz, Exciton binding energy and nonhydrogenic Rydberg series in monolayer WS<sub>2</sub>, *Physical Review Letters* **113**, 076802 (2014).
- [14] P. Cudazzo, I. V. Tokatly, and A. Rubio, Dielectric screening in two-dimensional insulators: Implications for excitonic and impurity states in graphane, *Physical Review B* **84**, 085406 (2011).
- [15] L. V. Keldysh, Coulomb interaction in thin semiconductor and semimetal films, in *Selected Papers of Leonid V Keldysh* (World Scientific, 2024) pp. 155–158.
- [16] E. Prada, J. V. Alvarez, K. L. Narasimha-Acharya, F. J. Bailer, and J. J. Palacios, Effective-mass theory for the anisotropic exciton in two-dimensional crystals: Application to phosphorene, *Physical Review B* **91**, 245421 (2015).
- [17] J. N. S. Gomes, C. Trallero-Giner, and M. I. Vasilevskiy, Variational calculation of the lowest exciton states in phosphorene and transition metal dichalcogenides, *Journal of Physics: Condensed Matter* **34**, 045702 (2021).
- [18] P. Hohenberg, Inhomogeneous electron gas, *Physical Review* **136**, B864 (1964).
- [19] W. Kohn, Self-consistent equations including exchange and correlation effects, *Physical Review* **140**, A1133 (1965).
- [20] H. Bruus and K. Flensberg, *Many-body quantum theory in condensed matter physics - an introduction* (Oxford University Press, 2004).
- [21] M. S. Hybertsen, Electron correlation in semiconductors and insulators: Band gaps and quasiparticle energies, *Physical Review B* **34**, 5390–5413 (1986).
- [22] R. M. Martin, L. Reining, and D. M. Ceperley, *Interacting Electrons: Theory and Computational Approaches* (Cambridge University Press, 2016).
- [23] M. Rohlfing and S. G. Louie, Electron-hole excitations and optical spectra from first principles, *Physical Review B* **62**, 4927 (2000).
- [24] D. Y. Qiu, *Many-body Effects on the Quasiparticle and Optical Properties of Quasi-two-dimensional Systems*, Ph.D. thesis, University of California, Berkeley (2017).
- [25] F. Homrich da Jornada, *Quasiparticle and Optical Properties of Quasi-Two-Dimensional Systems*, Ph.D. thesis, University of California, Berkeley (2017).
- [26] E. Ridolfi, C. H. Lewenkopf, and V. M. Pereira, Excitonic structure of the optical conductivity in MoS<sub>2</sub> monolayers, *Physical Review B* **97**, 205409 (2018).
- [27] T. Galvani, F. Paleari, H. P. C. Miranda, A. Molina-Sánchez, L. Wirtz, S. Latil, H. Amara, and F. Ducastelle, Excitons in boron nitride single layer, *Physical Review B* **94**, 125303 (2016).
- [28] A. J. Uría-Álvarez, J. J. Esteve-Paredes, M. A. García-Blázquez, and J. J. Palacios, Efficient computation of optical excitations in two-dimensional materials with the Xatu code, *Computer Physics Communications* **295**, 109001 (2024).
- [29] J. C. G. Henriques, I. Epstein, and N. M. R. Peres, Absorption and optical selection rules of tunable excitons in biased bilayer graphene, *Physical Review B* **105**, 045411 (2022).

- [30] M. F. C. M. Quintela, J. C. G. Henriques, L. G. M. Tenório, and N. M. R. Peres, Theoretical methods for excitonic physics in 2D materials, *physica status solidi (b)* **259**, 2200097 (2022).
- [31] G. H. Wannier, The structure of electronic excitation levels in insulating crystals, *Physical Review* **52**, 191 (1937).
- [32] E. I. Blount, Formalisms of band theory (Academic Press, 1962) pp. 305–373.
- [33] J. C. G. Henriques, G. B. Ventura, C. D. M. Fernandes, and N. M. R. Peres, Optical absorption of single-layer hexagonal boron nitride in the ultraviolet, *Journal of Physics: Condensed Matter* **32**, 025304 (2019).
- [34] A. Erba, J. K. Desmarais, S. Casassa, B. Civalleri, L. Donà, I. J. Bush, B. Searle, L. Maschio, L. Edith-Daga, A. Cossard, C. Ribaldone, E. Ascrizzi, N. L. Marana, J.-P. Flament, and B. Kirtman, Crystal23: A program for computational solid state physics and chemistry, *Journal of Chemical Theory and Computation* **19**, 6891–6932 (2023).
- [35] J. Heyd, G. E. Scuseria, and M. Ernzerhof, Hybrid functionals based on a screened Coulomb potential, *The Journal of Chemical Physics* **118**, 8207 (2003).
- [36] K. S. Thygesen, Calculating excitons, plasmons, and quasiparticles in 2D materials and van der Waals heterostructures, *2D Materials* **4**, 022004 (2017).
- [37] J. Deslippe, G. Samsonidze, D. A. Strubbe, M. Jain, M. L. Cohen, and S. G. Louie, BerkeleyGW: A massively parallel computer package for the calculation of the quasiparticle and optical properties of materials and nanostructures, *Computer Physics Communications* **183**, 1269–1289 (2012).
- [38] J. J. Mortensen, A. H. Larsen, M. Kuisma, A. V. Ivanov, A. Taghizadeh, A. Peterson, A. Haldar, A. O. Dohn, C. Schäfer, E. Ö. Jónsson, E. D. Hermes, F. A. Nilsson, G. Kastlunger, G. Levi, H. Jónsson, H. Häkkinen, J. Fojt, J. Kangsabanik, J. Sødequist, J. Lehtomäki, J. Heske, J. Enkovaara, K. T. Winther, M. Dulak, M. M. Melander, M. Ovesen, M. Louhivuori, M. Walter, M. Gjerding, O. Lopez-Acevedo, P. Erhart, R. Warmbier, R. Würdemann, S. Kaappa, S. Latini, T. M. Boland, T. Bligaard, T. Skovhus, T. Susi, T. Maxson, T. Rossi, X. Chen, Y. L. A. Schmerwitz, J. Schiøtz, T. Olsen, K. W. Jacobsen, and K. S. Thygesen, GPAW: An open Python package for electronic structure calculations, *The Journal of Chemical Physics* **160**, 092503 (2024).
- [39] A. Marini, C. Hogan, M. Grüning, and D. Varsano, yambo: An *ab initio* tool for excited state calculations, *Computer Physics Communications* **180**, 1392–1403 (2009).
- [40] S. Latini, T. Olsen, and K. S. Thygesen, Excitons in van der Waals heterostructures: The important role of dielectric screening, *Physical Review B* **92**, 245123 (2015).
- [41] F. Hüser, T. Olsen, and K. S. Thygesen, How dielectric screening in two-dimensional crystals affects the convergence of excited-state calculations: Monolayer MoS<sub>2</sub>, *Physical Review B* **88**, 245309 (2013).
- [42] K. Andersen, S. Latini, and K. S. Thygesen, Dielectric genome of van der Waals heterostructures, *Nano Letters* **15**, 4616–4621 (2015).
- [43] N. S. Rytova, The screened potential of a point charge in a thin film, *Moscow University Physics Bulletin* **3**, 18 (1967).
- [44] M. L. Trolle, T. G. Pedersen, and V. Vénard, Model dielectric function for 2D semiconductors including substrate screening, *Scientific Reports* **7**, 39844 (2017).
- [45] P. Li and I. Appelbaum, Excitons without effective mass: Biased bilayer graphene, *Physical Review B* **99**, 035429 (2019).
- [46] M. F. C. M. Quintela, N. M. R. Peres, and T. G. Pedersen, Tunable nonlinear excitonic optical response in biased bilayer graphene, *Physical Review B* **110**, 085433 (2024).
- [47] Y.-S. Huang, Y.-H. Chan, and G.-Y. Guo, Large shift currents via in-gap and charge-neutral excitons in a monolayer and nanotubes of BN, *Physical Review B* **108**, 075413 (2023).
- [48] F. Zhang, C. S. Ong, J. W. Ruan, M. Wu, X. Q. Shi, Z. K. Tang, and S. G. Louie, Intervalley excitonic hybridization, optical selection rules, and imperfect circular dichroism in monolayer *h*-BN, *Physical Review Letters* **128**, 047402 (2022).
- [49] M. A. García-Blázquez and J. J. Palacios, First-principles excitons in periodic systems with Gaussian density fitting and Ewald potential functions, *Physical Review Research* **7**, 013156 (2025).
- [50] H. M. Hill, A. F. Rigosi, C. Roquelet, A. Chernikov, T. C. Berkelbach, D. R. Reichman, M. S. Hybertsen, L. E. Brus, and T. F. Heinz, Observation of excitonic Rydberg states in monolayer MoS<sub>2</sub> and WS<sub>2</sub> by photoluminescence excitation spectroscopy, *Nano Letters* **15**, 2992–2997 (2015).
- [51] S. L. Adler, Quantum theory of the dielectric constant in real solids, *Physical Review* **126**, 413–420 (1962).
- [52] N. Wiser, Dielectric constant with local field effects included, *Physical Review* **129**, 62–69 (1963).
- [53] R. M. Martin, *Electronic Structure: Basic Theory and Practical Methods* (Cambridge University Press, 2004).
- [54] J. Kohanoff, *Electronic Structure Calculations for Solids and Molecules: Theory and Computational Methods* (Cambridge University Press, Cambridge, 2006).
- [55] M. Liu, A. Gopakumar, V. I. Hegde, J. He, and C. Wolverton, High-throughput hybrid-functional DFT calculations of bandgaps and formation energies and multifidelity learning with uncertainty quantification, *Physical Review Materials* **8**, 043803 (2024).
- [56] J. P. Perdew, K. Burke, and M. Ernzerhof, Generalized gradient approximation made simple, *Physical Review Letters* **77**, 3865 (1996).
- [57] E. H. Hwang and S. Das Sarma, Dielectric function, screening, and plasmons in two-dimensional graphene, *Physical Review B* **75**, 205418 (2007).
- [58] T. Sohler, M. Calandra, and F. Mauri, Density-functional calculation of static screening in two-dimensional materials: The long-wavelength dielectric function of graphene, *Physical Review B* **91**, 165428 (2015).
- [59] P. Ninhos, C. Tserkezis, N. A. Mortensen, and N. M. R. Peres, Tunable exciton polaritons in band-gap engineered hexagonal boron nitride, *ACS Nano* **18**, 20751–20761 (2024).
- [60] J. C. G. Henriques, B. Amorim, R. M. Ribeiro, and N. M. R. Peres, Excitonic response of AA' and AB stacked hBN bilayers, *Physical Review B* **105**, 115421 (2022).
- [61] J. C. G. Henriques and N. M. R. Peres, Excitons in phosphorene: A semi-analytical perturbative approach, *Physical Review B* **101**, 035406 (2020).

- [62] A. Baldereschi and E. Tosatti, Mean-value point and dielectric properties of semiconductors and insulators, *Physical Review B* **17**, 4710–4717 (1978).
- [63] F. A. Rasmussen, P. S. Schmidt, K. T. Winther, and K. S. Thygesen, Efficient many-body calculations for two-dimensional materials using exact limits for the screened potential: Band gaps of MoS<sub>2</sub>, h-BN, and phosphorene, *Physical Review B* **94**, 155406 (2016).
- [64] M. Shishkin and G. Kresse, Implementation and performance of the frequency-dependent *GW* method within the PAW framework, *Physical Review B* **74**, 035101 (2006).
- [65] In the continuously translational invariant case, these effects are not present, and in that case, the microscopic and macroscopic dielectric functions coincide.
- [66] K. Huang, *Statistical Mechanics, 2nd Edition* (Wiley, 1987).
- [67] G. Grosso and G. P. Parravicini, Excitons, plasmons, and dielectric screening in crystals, in *Solid State Physics*, edited by G. Grosso and G. P. Parravicini (Academic Press, Amsterdam, 2014) Chap. 7, p. 287–331, 2nd ed.

# Computation of excitons in two-dimensional materials with screened interactions beyond classical models

–SUPPORTING INFORMATION–

Pedro Ninhos<sup>1</sup>, Alejandro José Uría-Álvarez<sup>3,4,5</sup>, Christos Tserkezis<sup>1</sup>,  
N. Asger Mortensen<sup>1,2</sup>, and Juan José Palacios<sup>3,4\*</sup>

<sup>1</sup>POLIMA—Center for Polariton-driven Light–Matter Interactions, University of Southern Denmark, Campusvej 55, DK-5230 Odense M, Denmark

<sup>2</sup>D-IAS—Danish Institute for Advanced Study, University of Southern Denmark, Campusvej 55, DK-5230 Odense M, Denmark

<sup>3</sup>Departamento de Física de la Materia Condensada, Universidad Autónoma de Madrid, Madrid, Spain

<sup>4</sup>Condensed Matter Physics Center (IFIMAC) and Instituto Nicolás Cabrera (INC), Universidad Autónoma de Madrid, 28049 Madrid, Spain

<sup>5</sup>Departamento de Física, Universidad de Oviedo, 33007 Oviedo, Spain

\*@uam.es

## S.1 Non-interacting polarizability and Time-Reversal Symmetry

In this section we derive expression (1) in the main text from its more general form in equation (5), by taking the static limit  $\omega \rightarrow 0$  and assuming the system is time-reversal symmetric. In a periodic system with no contribution to the Hamiltonian that violates time-reversal symmetry (TRS), such as all the ones considered in this work, there exists a unitary transformation  $T$  such that

$$TH^*(-\mathbf{k})T^\dagger = H(\mathbf{k}) \quad (\text{S.1})$$

is verified for the Bloch Hamiltonian  $H(\mathbf{k})$ . Also, for time-reversal invariant systems, the quasiparticle energies naturally obey  $\epsilon_{n,\mathbf{k}} = \epsilon_{n,-\mathbf{k}}$ .

The expression (5) in the main text for the polarizability in the static and zero absolute temperature limits evaluates to

$$\begin{aligned} \chi_{\mathbf{G}\mathbf{G}'}^0(\mathbf{q}; \omega = 0) = & \frac{1}{N} \sum_{vc,\mathbf{k}\sigma} \left[ \frac{\langle c, \mathbf{k} | e^{-i(\mathbf{q}+\mathbf{G})\cdot\mathbf{r}} | v, \mathbf{k} + \mathbf{q} \rangle \langle v, \mathbf{k} + \mathbf{q} | e^{i(\mathbf{q}+\mathbf{G}')\cdot\mathbf{r}} | c, \mathbf{k} \rangle}{\epsilon_{v,\mathbf{k}+\mathbf{q}} - \epsilon_{c,\mathbf{k}}} \right] + \\ & \frac{1}{N} \sum_{vc,\mathbf{k}\sigma} \left[ \frac{\langle v, \mathbf{k} | e^{-i(\mathbf{q}+\mathbf{G})\cdot\mathbf{r}} | c, \mathbf{k} + \mathbf{q} \rangle \langle c, \mathbf{k} + \mathbf{q} | e^{i(\mathbf{q}+\mathbf{G}')\cdot\mathbf{r}} | v, \mathbf{k} \rangle}{\epsilon_{v,\mathbf{k}} - \epsilon_{c,\mathbf{k}+\mathbf{q}}} \right]. \end{aligned} \quad (\text{S.2})$$

Note that in the previous expression we only account for single-particle state transitions from a valence band and to a conduction band, or vice-versa. In other words, since we are working with pristine undoped semiconductors/insulators, there is no intraband contribution to the polarizability, contrary to metallic systems where intraband transitions are allowed besides the interband ones.

Now we show that the second term on the right-hand side (RHS) of the previous expression equals the first one. First, we recall that the sum over momentum  $\mathbf{k}$  is over momenta in the Brillouin zone (BZ), which is centrosymmetric. Therefore, we can replace  $\mathbf{k} \rightarrow -\mathbf{k}$ , and then we shift  $\mathbf{k} \rightarrow \mathbf{k} + \mathbf{q}$  to obtain

$$\begin{aligned}
& \sum_{v,c,\mathbf{k}\sigma} \frac{\langle v, -\mathbf{k} - \mathbf{q} | e^{-i(\mathbf{q}+\mathbf{G})\cdot\mathbf{r}} | c, -\mathbf{k} \rangle \langle c, -\mathbf{k} | e^{i(\mathbf{q}+\mathbf{G}')\cdot\mathbf{r}} | v, -\mathbf{k} - \mathbf{q} \rangle}{\epsilon_{v,-\mathbf{k}-\mathbf{q}} - \epsilon_{c,-\mathbf{k}}} = \\
& \sum_{v,c,\mathbf{k}\sigma} \frac{\langle v, -\mathbf{k} - \mathbf{q} | e^{-i(\mathbf{q}+\mathbf{G})\cdot\mathbf{r}} | c, -\mathbf{k} \rangle \langle c, -\mathbf{k} | e^{i(\mathbf{q}+\mathbf{G}')\cdot\mathbf{r}} | v, -\mathbf{k} - \mathbf{q} \rangle}{\epsilon_{v,\mathbf{k}+\mathbf{q}} - \epsilon_{c,\mathbf{k}}} =
\end{aligned} \tag{S.3}$$

where we used TRS to write the equality, namely  $\epsilon_{n,\mathbf{k}} = \epsilon_{n,-\mathbf{k}}$ . Now, we only need some sort of symmetry for the plane-wave matrix elements of the form  $\langle n, \mathbf{k} | e^{-i\mathbf{q}\cdot\mathbf{r}} | n', \mathbf{k}' \rangle$ . For that, we revisit their expression (7) from the main text, which is written in terms of the tight-binding coefficients composing the eigenvectors of the Bloch Hamiltonian,  $\mathbf{C}^{n\mathbf{k}}$ . As eigenvectors of the Bloch Hamiltonian, they obey

$$\begin{aligned}
H(\mathbf{k})\mathbf{C}^{n,\mathbf{k}} = \epsilon_{n,\mathbf{k}}\mathbf{C}^{n,\mathbf{k}} &\Leftrightarrow H(-\mathbf{k})\mathbf{C}^{n,-\mathbf{k}} = \epsilon_{n,-\mathbf{k}}\mathbf{C}^{n,-\mathbf{k}} \Leftrightarrow \\
\Leftrightarrow H^*(-\mathbf{k})(\mathbf{C}^{n,-\mathbf{k}})^* &= \epsilon_{n,\mathbf{k}}(\mathbf{C}^{n,-\mathbf{k}})^* \Leftrightarrow TH^*(-\mathbf{k})T^\dagger T(\mathbf{C}^{n,-\mathbf{k}})^* = \epsilon_{n,-\mathbf{k}}T(\mathbf{C}^{n,-\mathbf{k}})^* \Leftrightarrow \\
&\Leftrightarrow H(\mathbf{k})T(\mathbf{C}^{n,-\mathbf{k}})^* = \epsilon_{n,\mathbf{k}}T(\mathbf{C}^{n,-\mathbf{k}})^*,
\end{aligned} \tag{S.4}$$

where to get the last equality we used the identities verified by  $H(\mathbf{k})$  and  $\epsilon_{n,\mathbf{k}}$  introduced above. So, in principle, we have  $T(\mathbf{C}^{n,-\mathbf{k}})^* = \mathbf{C}^{n,\mathbf{k}}$ .

Now, for the matrix elements of interest, we introduce the following notation:

$$\langle n, \mathbf{k} | e^{-i(\mathbf{k}'-\mathbf{k}+\mathbf{G})\cdot\mathbf{r}} | n', \mathbf{k}' \rangle = \sum_{i\alpha} (C_{i\alpha}^{n\mathbf{k}})^* C_{i\alpha}^{n'\mathbf{k}'} e^{-i(\mathbf{k}'-\mathbf{k}+\mathbf{G})\cdot\mathbf{t}_i} \equiv (\mathbf{C}^{n,\mathbf{k}})^\dagger \cdot (\mathbf{C}^{n',\mathbf{k}'} \odot \underline{\phi}) \tag{S.5}$$

where the vector  $\underline{\phi}$  has by entries the phases  $e^{-i(\mathbf{k}'-\mathbf{k}+\mathbf{G})\cdot\mathbf{t}_i}$ , that is,  $(\underline{\phi})_{i\alpha} = e^{-i(\mathbf{k}'-\mathbf{k}+\mathbf{G})\cdot\mathbf{t}_i}$ , and  $\odot$  is used to denote element-wise product, usually called the Hadamard product in the literature. Then, we only need to apply the identity  $T(\mathbf{C}^{n,-\mathbf{k}})^* = \mathbf{C}^{n,\mathbf{k}}$  to obtain

$$\begin{aligned}
\langle n, \mathbf{k} | e^{-i(\mathbf{k}'-\mathbf{k}+\mathbf{G})\cdot\mathbf{r}} | n', \mathbf{k}' \rangle &= (\mathbf{C}^{n,\mathbf{k}})^\dagger \cdot (\mathbf{C}^{n',\mathbf{k}'} \odot \underline{\phi}) = \left( (\mathbf{C}^{n,-\mathbf{k}})^\top T^\dagger \right) \cdot \left( (T(\mathbf{C}^{n',-\mathbf{k}'})^*) \odot \underline{\phi} \right) = \\
&= (\mathbf{C}^{n,-\mathbf{k}})^\top (T^\dagger T) \left( (\mathbf{C}^{n',-\mathbf{k}'})^* \odot \underline{\phi} \right) = (\mathbf{C}^{n',-\mathbf{k}'})^\dagger \cdot (\mathbf{C}^{n,-\mathbf{k}} \odot \underline{\phi}) = \\
&= \langle n', -\mathbf{k}' | e^{-i(\mathbf{k}'-\mathbf{k}+\mathbf{G})\cdot\mathbf{r}} | n, -\mathbf{k} \rangle, \text{ with } \top \text{ denoting transpose.}
\end{aligned} \tag{S.6}$$

In this way, the second term in the polarizability can be rewritten as

$$\begin{aligned}
& \sum_{v,c,\mathbf{k}\sigma} \frac{\langle v, -\mathbf{k} - \mathbf{q} | e^{-i(\mathbf{q}+\mathbf{G})\cdot\mathbf{r}} | c, -\mathbf{k} \rangle \langle c, -\mathbf{k} | e^{i(\mathbf{q}+\mathbf{G}')\cdot\mathbf{r}} | v, -\mathbf{k} - \mathbf{q} \rangle}{\epsilon_{v,\mathbf{k}+\mathbf{q}} - \epsilon_{c,\mathbf{k}}} = \\
& \sum_{v,c,\mathbf{k}\sigma} \frac{\langle c, \mathbf{k} | e^{-i(\mathbf{q}+\mathbf{G})\cdot\mathbf{r}} | v, \mathbf{k} + \mathbf{q} \rangle \langle v, \mathbf{k} + \mathbf{q} | e^{i(\mathbf{q}+\mathbf{G}')\cdot\mathbf{r}} | c, \mathbf{k} \rangle}{\epsilon_{v,\mathbf{k}+\mathbf{q}} - \epsilon_{c,\mathbf{k}}},
\end{aligned} \tag{S.7}$$

which concludes our proof. This identity has also been verified numerically.

## S.2 Analysis of the inverse dielectric matrix

In Fig. S1, we display the results for the convergence of few inverse dielectric matrix elements, considering the two materials we studied separately in the main text. Panels **a-d** on the left side correspond to hBN, while those on the right, **e-h**, correspond to MoS<sub>2</sub>. We observe, in each panel, how fast each matrix element converges with the number of vectors  $\mathbf{G}$  included. For both materials we observe a very slow convergence (if they do converge at all), which has the consequence of increased computational-effort requirements.

By making a comparison between these two materials, even though the characteristic curves for the convergence seem similar, for MoS<sub>2</sub> one needs to include fewer reciprocal lattice vectors to achieve a convergence similar to the one of hBN. That might be simply due to the fact that MoS<sub>2</sub> has a lattice parameter larger than that of hBN, around 3.16 Å compared to 2.51 Å for these two materials,

respectively. This is equivalent to saying that the unit cell of MoS<sub>2</sub> is larger than that of hBN. In turn, this implies that hBN has a larger BZ than MoS<sub>2</sub>, whence longer primitive reciprocal lattice vectors than MoS<sub>2</sub>. Longer  $\mathbf{G}$  vectors correspond to slower oscillations of the form  $\exp[i(\mathbf{q} + \mathbf{G}) \cdot \mathbf{r}]$ . Therefore, to account for all the fast oscillations within a length of the order of the unit cell, one has to include more reciprocal lattice vectors for hBN than for MoS<sub>2</sub>.

Before computing the exciton, one has to first compute the inverse dielectric matrix at each point in the BZ. To understand how its elements behave with momentum, we display in Fig. S2 few selected components of the inverse dielectric function as a function of momentum  $q = |\mathbf{q}|$  taken along the high-symmetry line  $\Gamma - K$ . There we can observe a feature of the head matrix element in panels **a** and **c** (red curves), for hBN and MoS<sub>2</sub> respectively, which is its sharp linear dependence near the origin, something that has been documented before in Ref. [4]. In that same reference, it was observed that a selected diagonal element of the body presents almost no dispersive behavior, in very close similarity to what we see in panels **a** and **c** (blue curves). Still in the same figure, in panels **b** and **d** we observe for the selected wing elements that even though they are dispersive, they are so on a much smaller scale when compared to the material's corresponding head matrix element (note the scaling factor of ten in panel **b**). Something identical has been observed in Ref. [4], where the head element presents a strong dispersion when compared to a wing element. We note also that the results presented in Ref. [4] for the matrix elements of the inverse dielectric function were obtained by first-principle calculations, making the similarity of the results obtained between *ab initio* approaches and our second-principles approach quite notable. A similar behavior for the dispersion of the head matrix element of MoS<sub>2</sub> can be seen in a work by Hüser *et al.* [5], and another one for GaN sheets has been reported by Ismail-Beigi [6] with the same characteristic dependence, in both works with standard DFT calculations followed by *GW* corrections.

### S.3 Long-wavelength limit of the dielectric function and screened potential

In this section we explain in detail how the divergences of the dielectric matrix in the long-wavelength limit  $\mathbf{q} \rightarrow \mathbf{0}$  are treated in this work. As commonly done in the literature, different matrix elements of the dielectric function have different treatments, namely the head  $\varepsilon_{\mathbf{00}}$ , the wing  $\varepsilon_{\mathbf{G0}}$  and  $\varepsilon_{\mathbf{0G}}$  with  $\mathbf{G} \neq \mathbf{0}$ , which are the problematic ones. As is equally common in the literature, we adopt the symmetrized dielectric matrix defined by

$$\varepsilon_{\mathbf{GG}'}(\mathbf{q}) = \delta_{\mathbf{GG}'} - \sqrt{v_c(\mathbf{q} + \mathbf{G})} \chi_{\mathbf{GG}'}^0(\mathbf{q}) \sqrt{v_c(\mathbf{q} + \mathbf{G}')}, \quad (\text{S.8})$$

which avoids technical issues in the near-zero  $\mathbf{q}$  limit, as we explain next. For the head element, it actually does not matter whether we symmetrize the dielectric function, since<sup>1</sup>

$$\begin{aligned} \varepsilon_{\mathbf{00}}(\mathbf{q} \rightarrow \mathbf{0}) &= 1 - \sqrt{v_c(\mathbf{q} \rightarrow \mathbf{0})} \chi_{\mathbf{00}}^0(\mathbf{q} \rightarrow \mathbf{0}) \sqrt{v_c(\mathbf{q} \rightarrow \mathbf{0})} = 1 - v_c(\mathbf{q} \rightarrow \mathbf{0}) \chi_{\mathbf{00}}^0(\mathbf{q} \rightarrow \mathbf{0}) = \\ &= 1 - \frac{e}{2\varepsilon_0 q} \mathbf{q} \cdot \mathbf{B} \mathbf{q} \rightarrow 1, \end{aligned} \quad (\text{S.9})$$

where the last equality holds for very small  $\mathbf{q}$ , and  $\mathbf{B}$  is the Hessian matrix of the function  $\chi_{\mathbf{00}}^0(q_x, q_y)$  at the point  $(q_x, q_y) = (0, 0)$ . The Hessian, here a 2 by 2 matrix, does not depend on the small vector, because the function  $\chi_{\mathbf{00}}^0(\mathbf{q})$  is analytic in  $\mathbf{q}$  around the origin, as stated by Pick, Cohen and Martin in [9]. In the same paper, they explain that actually all the functions  $\chi_{\mathbf{GG}'}^0(\mathbf{q})$  for  $\mathbf{G}$  and  $\mathbf{G}'$  zero or not are analytic at  $\mathbf{q} = \mathbf{0}$ . In other words, the functions  $\chi_{\mathbf{GG}'}^0(\mathbf{q})$  can be expanded around the origin in powers of  $\mathbf{q}$  (in other words, it admits a Taylor expansion). Therefore, we can write for the wing terms

$$\varepsilon_{\mathbf{G0}}(\mathbf{q} \rightarrow \mathbf{0}) = -\sqrt{v_c(\mathbf{G})} \chi_{\mathbf{G0}}^0(\mathbf{q} \rightarrow \mathbf{0}) \sqrt{v_c(\mathbf{q} \rightarrow \mathbf{0})} = -\frac{e}{2\varepsilon_0 \sqrt{|\mathbf{G}|} \sqrt{q}} \mathbf{q} \cdot \mathbf{A}(\mathbf{G}) \propto \sqrt{q} \rightarrow 0, \quad (\text{S.10})$$

$$\varepsilon_{\mathbf{0G}}(\mathbf{q} \rightarrow \mathbf{0}) = -\sqrt{v_c(\mathbf{q} \rightarrow \mathbf{0})} \chi_{\mathbf{0G}}^0(\mathbf{q} \rightarrow \mathbf{0}) \sqrt{v_c(\mathbf{G})} = -\frac{e}{2\varepsilon_0 \sqrt{|\mathbf{G}|} \sqrt{q}} \mathbf{q} \cdot \mathbf{A}(\mathbf{G})^* \propto \sqrt{q} \rightarrow 0, \quad (\text{S.11})$$

<sup>1</sup>Let us cast the unit cell area factor  $\Omega_{\text{UC}}$  appearing in the expression for the Coulomb potential defined in the main text to  $\chi^0$ , as that factor is not relevant for the discussion.

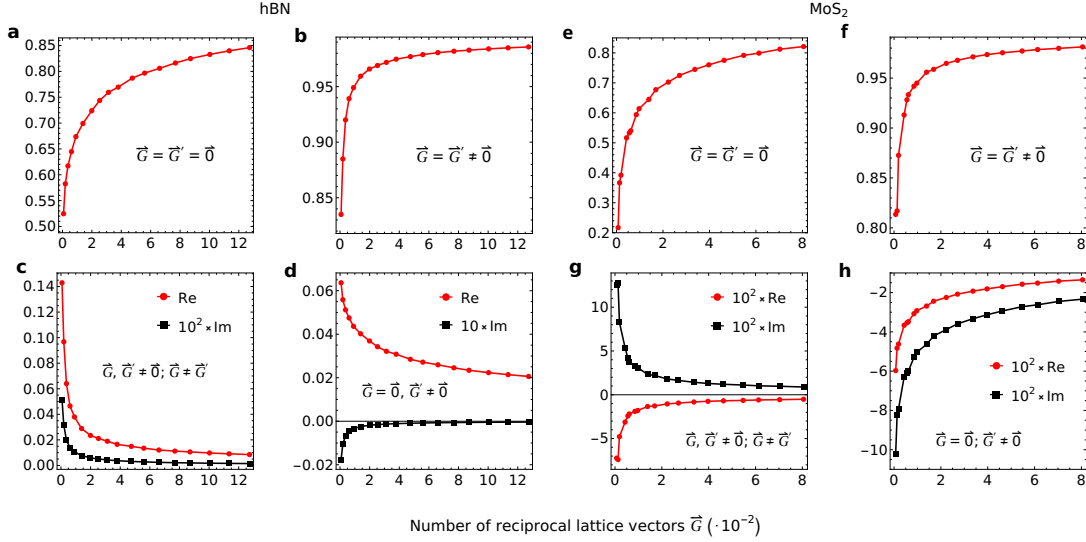


Figure S1: **Convergence of the inverse dielectric matrix with the number of reciprocal lattice vectors.** Convergence of a few selected inverse dielectric function matrix elements  $\varepsilon_{\vec{G}\vec{G}'}^{-1}(\mathbf{q})$  at the wavevector  $\mathbf{q} = (0.2, 0) \text{ \AA}^{-1}$ . Panels **a-d** are for hBN and panels **e-h** for MoS<sub>2</sub>. Panels **a** and **e** represent the head matrix element for hBN and MoS<sub>2</sub>, respectively. Panels **b,f** correspond to diagonal matrix elements. Panels **c,g** show an off-diagonal matrix element that is not a wing one. Finally, panels **d,h** show a wing matrix element. For hBN, the cut-off goes up to  $G_c^\varepsilon = 52 \text{ \AA}^{-1}$ , corresponding to 1273 vectors, while for MoS<sub>2</sub> it goes up to  $G_c^\varepsilon = 34 \text{ \AA}^{-1}$ , corresponding to 805 vectors.

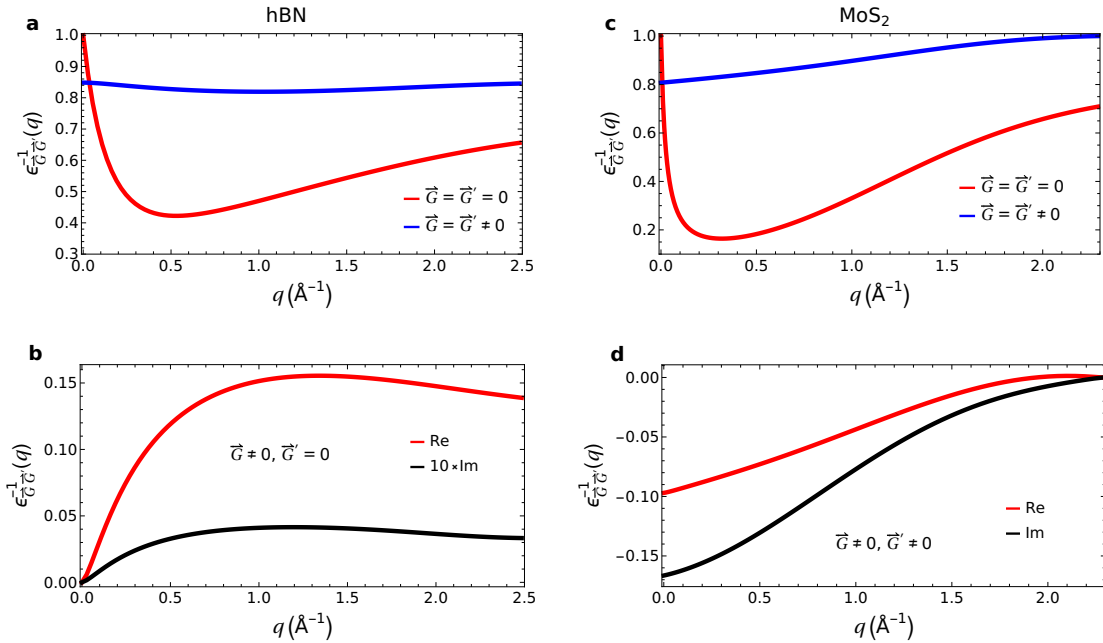


Figure S2: **Dispersion of the inverse dielectric function.** Matrix elements of the inverse dielectric function as a function of momentum, considering hBN on the left and MoS<sub>2</sub> on the right. Panels **a,c** show two diagonal elements, the head and the first one in the body, corresponding to a primitive reciprocal lattice vector  $\mathbf{G}$ . Panels **b,d** show a wing matrix element, for the same reciprocal lattice vector  $\mathbf{G}$ . We used  $G_c^\varepsilon = 3 \text{ \AA}^{-1}$  as a cutoff for the reciprocal lattice vectors for both materials.

where  $\mathbf{A}(\mathbf{G})$  is the Jacobian matrix (vector, actually) of the function  $\chi_{\mathbf{G}\mathbf{0}}^0(\mathbf{q})$  at  $\mathbf{q} = \mathbf{0}$ , that does not depend on  $\mathbf{q}$  due to  $\chi_{\mathbf{G}\mathbf{0}}^0(\mathbf{q})$  being analytic, as mentioned above.

If we were to use the non-symmetric dielectric matrix, then the wing terms  $\varepsilon_{\mathbf{G}\mathbf{0}}$  would also tend to zero as  $\mathbf{q} \rightarrow \mathbf{0}$ , but with  $q$  instead, but the terms  $\varepsilon_{\mathbf{0}\mathbf{G}}$  would tend to  $\varepsilon_{\mathbf{0}\mathbf{G}}(\mathbf{q} \rightarrow \mathbf{0}) \rightarrow -e\hat{\mathbf{q}} \cdot \mathbf{A}(\mathbf{G})^*/2\varepsilon_0$ , which is finite and depends on the direction along which one takes the limit  $\mathbf{q} \rightarrow \mathbf{0}$ . We can see the usefulness of using the symmetrized dielectric matrix, making it easier to implement numerically. One just sets  $\varepsilon_{\mathbf{0}\mathbf{G}}(\mathbf{0}) = \varepsilon_{\mathbf{G}\mathbf{0}}(\mathbf{0}) = 0$ , leaving an eventual long-wavelength regularization for later when dealing with the screened potential.

Now, we try to determine the behavior of the inverse dielectric matrix near  $\mathbf{q} = \mathbf{0}$ , just as done in Refs. [10] and [9], so that we know how to regularize the singular terms of the screened Coulomb potential, needed for the excitons. We write the dielectric matrix as a matrix by blocks, separating the head, the wing, and the body terms that we denote by  $\varepsilon_{\mathbf{0}\mathbf{0}}$ ,  $\varepsilon_{\mathbf{G}\mathbf{0}}$  and  $\varepsilon_{\mathbf{0}\mathbf{G}}$ , and  $B_{\mathbf{G}\mathbf{G}'}$ , respectively. Skipping the details of the inversion, we directly write

$$\varepsilon_{\mathbf{0}\mathbf{0}}^{-1} = \left[ \varepsilon_{\mathbf{0}\mathbf{0}} - \sum_{\mathbf{G}, \mathbf{G}' \neq \mathbf{0}} \varepsilon_{\mathbf{0}\mathbf{G}} B_{\mathbf{G}\mathbf{G}'}^{-1} \varepsilon_{\mathbf{G}'\mathbf{0}} \right]^{-1}, \quad (\text{S.12})$$

$$\varepsilon_{\mathbf{G}\mathbf{0}}^{-1} = -\varepsilon_{\mathbf{0}\mathbf{0}}^{-1} \sum_{\mathbf{G}' \neq \mathbf{0}} B_{\mathbf{G}\mathbf{G}'}^{-1} \varepsilon_{\mathbf{G}'\mathbf{0}}, \quad (\text{S.13})$$

$$\varepsilon_{\mathbf{0}\mathbf{G}}^{-1} = -\varepsilon_{\mathbf{0}\mathbf{0}}^{-1} \sum_{\mathbf{G}' \neq \mathbf{0}} \varepsilon_{\mathbf{0}\mathbf{G}'} B_{\mathbf{G}'\mathbf{G}}^{-1}, \quad (\text{S.14})$$

$$\varepsilon_{\mathbf{G}\mathbf{G}'}^{-1} = B_{\mathbf{G}\mathbf{G}'}^{-1} + \varepsilon_{\mathbf{0}\mathbf{0}}^{-1} \left( \sum_{\mathbf{G}'' \neq \mathbf{0}} B_{\mathbf{G}\mathbf{G}''}^{-1} \varepsilon_{\mathbf{G}''\mathbf{0}} \right) \left( \sum_{\mathbf{G}'' \neq \mathbf{0}} \varepsilon_{\mathbf{0}\mathbf{G}''} B_{\mathbf{G}''\mathbf{G}'}^{-1} \right). \quad (\text{S.15})$$

Please note that in the previous relations,  $B_{\mathbf{G}\mathbf{G}'}^{-1}$  designates the  $(\mathbf{G}, \mathbf{G}')$  matrix element of the inverse of the body, and not the inverse of the body element  $B_{\mathbf{G}\mathbf{G}'}$ . Given the properties of the wing matrix elements derived above when taking the long-wavelength limit, we can infer that

$$\varepsilon_{\mathbf{0}\mathbf{0}}^{-1}(\mathbf{q} \rightarrow \mathbf{0}) \rightarrow 1, \quad (\text{S.16})$$

$$\varepsilon_{\mathbf{G}\mathbf{G}'}^{-1}(\mathbf{q} \rightarrow \mathbf{0}) \rightarrow B_{\mathbf{G}\mathbf{G}'}^{-1}(\mathbf{q} \rightarrow \mathbf{0}), \quad (\text{S.17})$$

as one could expect for the head element of a strictly two-dimensional (2D) dielectric matrix, while the body of the inverse dielectric matrix is simply the inverse of the body of the dielectric matrix. However, the analysis of the wing elements needs more care, since we need to know how they behave for small  $\mathbf{q}$ . Using the very same properties of the wing elements  $\varepsilon_{\mathbf{G}\mathbf{0}}$  and  $\varepsilon_{\mathbf{0}\mathbf{G}}$ , we can write down

$$\varepsilon_{\mathbf{G}\mathbf{0}}^{-1}(\mathbf{q} \rightarrow \mathbf{0}) \rightarrow \sum_{\mathbf{G}' \neq \mathbf{0}} B_{\mathbf{G}\mathbf{G}'}^{-1} \frac{e}{2\varepsilon_0 \sqrt{G'}} \sqrt{q} \hat{\mathbf{q}} \cdot \mathbf{A}(\mathbf{G}') \rightarrow 0, \quad (\text{S.18})$$

$$\varepsilon_{\mathbf{0}\mathbf{G}}^{-1}(\mathbf{q} \rightarrow \mathbf{0}) \rightarrow \sum_{\mathbf{G}' \neq \mathbf{0}} B_{\mathbf{G}'\mathbf{G}}^{-1} \frac{e}{2\varepsilon_0 \sqrt{G'}} \sqrt{q} \hat{\mathbf{q}} \cdot \mathbf{A}(\mathbf{G}')^* \rightarrow 0, \quad (\text{S.19})$$

so the wing terms of the inverse dielectric matrix tend to zero when  $\mathbf{q}$  approaches zero, just as expected for a 2D system [4]. We are in a position now to address the troublesome matrix elements of the screened potential at zero momentum.

We know now that  $\varepsilon_{\mathbf{0}\mathbf{0}}^{-1}(\mathbf{q} \rightarrow \mathbf{0}) \rightarrow 1$  for small momentum, but the bare Coulomb potential diverges with  $1/q$ , whence the head term of the screened potential  $W_{\mathbf{0}\mathbf{0}}(\mathbf{q})$  diverges with  $1/q$  in the long-wavelength limit. Nonetheless, the  $\mathbf{q} = \mathbf{0}$  term in reciprocal-space calculations is known to be of upmost relevance to make calculations converge faster [10] and is known to behave like the Rytova-Keldysh potential for small  $\mathbf{q}$ . Therefore, one can come up with an analytical expression to regularize the term  $W_{\mathbf{0}\mathbf{0}}(\mathbf{0})$  as suggested by Hüser *et al.* in Ref. [5], where the divergent term is approximated by

$$W_{\mathbf{0}\mathbf{0}}(\mathbf{0}) = \frac{1}{\Omega_{\Gamma}} \int_{\Omega_{\Gamma}} d\mathbf{q} v_c(\mathbf{q}) [1 + \mathbf{q} \cdot \nabla_{\mathbf{q}} \varepsilon_{\mathbf{0}\mathbf{0}}^{-1}(\mathbf{q})|_{\mathbf{q}=\mathbf{0}}]. \quad (\text{S.20})$$

Knowing that the head element  $\varepsilon_{\mathbf{0}\mathbf{0}}^{-1}(\mathbf{q})$  approaches 1 linearly with  $q$  near the origin, we can find an analytical expression for the previous integral in terms of the gradient appearing inside the rectangular brackets, which can be readily evaluated numerically (see discussion around Eq. (25) in the main text). We can simply take  $\nabla_{\mathbf{q}} \varepsilon_{\mathbf{0}\mathbf{0}}^{-1}(\mathbf{q})|_{\mathbf{q}=\mathbf{0}} = (-r_0^x, -r_0^y)$ , where the parameters  $r_0^x$  and  $r_0^y$  are the screening parameters computed numerically along the  $x$  and  $y$  directions, respectively. The expression evaluates to

$$W_{\mathbf{0}\mathbf{0}}(\mathbf{0}) = \frac{e}{\varepsilon_0 q_0} \left[ 1 - \frac{1}{4} q_0 (r_0^x + r_0^y) \right] = \frac{e}{\varepsilon_0 q_0} \left( 1 - \frac{q_0 r_0}{2} \right), \quad (\text{S.21})$$

with the second equality holding for isotropic materials, and  $q_0$  is the radius of a small circle centered at the origin of the BZ, the high symmetry point  $\Gamma$ . Typically, for  $q_0$  we choose a percentage of around 40–50% of the magnitude of the  $\mathbf{k}$  point in the BZ mesh closest to the origin, denoted by  $k_0$  in the main text, which depends on the number of  $\mathbf{k}$  points used, and of course the geometry of the BZ. In the main text, we also denoted the percentage by  $\varsigma$ , so that  $q_0 = \varsigma k_0$ . The percentage is chosen by the user, while  $k_0$  is determined by the material model and the number of  $\mathbf{k}$  points chosen,  $N$ .

Regarding the wing terms of the screened potential using the symmetrized dielectric function, we get

$$W_{\mathbf{G}\mathbf{0}}(\mathbf{q} \rightarrow 0) = \sqrt{v_c(\mathbf{G})} \varepsilon_{\mathbf{G}\mathbf{0}}^{-1}(\mathbf{q} \rightarrow 0) \sqrt{v_c(\mathbf{q} \rightarrow 0)} = -\frac{e}{2\varepsilon_0 \sqrt{|\mathbf{G}|}} \hat{\mathbf{q}} \cdot \sum_{\mathbf{G}' \neq 0} \frac{1}{\sqrt{\mathbf{G}'}} \mathbf{A}(\mathbf{G}') B_{\mathbf{G}'\mathbf{G}}^{-1}, \quad (\text{S.22})$$

$$W_{\mathbf{0}\mathbf{G}}(\mathbf{q} \rightarrow 0) = \sqrt{v_c(\mathbf{q} \rightarrow 0)} \varepsilon_{\mathbf{0}\mathbf{G}}^{-1}(\mathbf{q} \rightarrow 0) \sqrt{v_c(\mathbf{G})} = -\frac{e}{2\varepsilon_0 \sqrt{|\mathbf{G}|}} \hat{\mathbf{q}} \cdot \sum_{\mathbf{G}' \neq 0} \frac{1}{\sqrt{\mathbf{G}'}} \mathbf{A}(\mathbf{G}')^* B_{\mathbf{G}'\mathbf{G}}^{-1}, \quad (\text{S.23})$$

with both results depending on the direction of the vector  $\mathbf{q}$  as it approaches zero in the same way. Even though they do not tend to a null value, they can be averaged around the origin, such that they become null upon averaging a centrosymmetric region (to account for eventual anisotropies). This is due to the fact that the dependence on the direction of the vector  $\mathbf{q}$  is linear in its versor  $\hat{\mathbf{q}} = \mathbf{q}/|\mathbf{q}|$ . This contrasts with the case of Rasmussen *et al.* [10], where the angular dependence of the wing terms of the screened potential is not trivial, in such a way that a numerical evaluation of the average has to be implemented. Therein, the head term depends non-trivially on  $\hat{\mathbf{q}}$  as well, but the simplicity of the expression allows for an approximate analytical expression.

The results of this section are summarized in Table S1.

Table S1: Summary of the behavior of the sensitive matrix elements of the dielectric function, of the inverse dielectric function and of the screened potential in the long-wavelength limit  $q \rightarrow 0$ . The head term of the screened potential demands a regularization scheme, while its wing terms will not contribute when averaged over a centrosymmetric region.

	Head ( $\mathbf{0}, \mathbf{0}$ )	Wing ( $\mathbf{G}, \mathbf{0}$ ) or ( $\mathbf{0}, \mathbf{G}$ )
$\varepsilon$	1	$\sqrt{q}$
$\varepsilon^{-1}$	1	$\sqrt{q}$
$W$	reg.	0

To finish the appendix, we would like to emphasize that the simplicity of the resulting non-zero contributions to the dielectric matrix, its inverse, and consequently the screened potential stem essentially from the slower divergence of the Coulomb potential in 2D, which goes with  $1/q$ , while in the 3D case commonly found in the literature one has  $v_c(q \rightarrow 0) \sim 1/q^2$ , making our numerical methods easier to implement and interpret.

## S.4 Comparison between models

In this section, we compare the results obtained for the dielectric function among different models for the same materials. We take the opportunity to also benchmark our results against more *ab initio* ones from the literature. Let us consider hBN first.

In Fig. S3, we plot the macroscopic 2D dielectric function computed through our 2D framework for the microscopic dielectric function alongside the *ab initio* ones in black. The continuous black curve was obtained in 2015 by Latini *et al.* [7], while the dashed black one was obtained by Rasmussen *et al.* [10] in 2016. The continuous black and dashed red curves have been presented already in the main text (see Fig. 4, Section IIC). The red curve, like explained in the main text, was obtained by applying a cutoff of  $G_c^\epsilon = 3 \text{ \AA}^{-1}$  to the reciprocal lattice vectors in the dielectric matrix. We show it once more to compare with the dashed black curve, which is more recent than the continuous black one, which we can also reproduce using our code if we apply the cutoff  $G_c^\epsilon = 5.1 \text{ \AA}^{-1}$  instead. This gives an extra confirmation that our theory for the dielectric function of 2D gapped materials is valid.

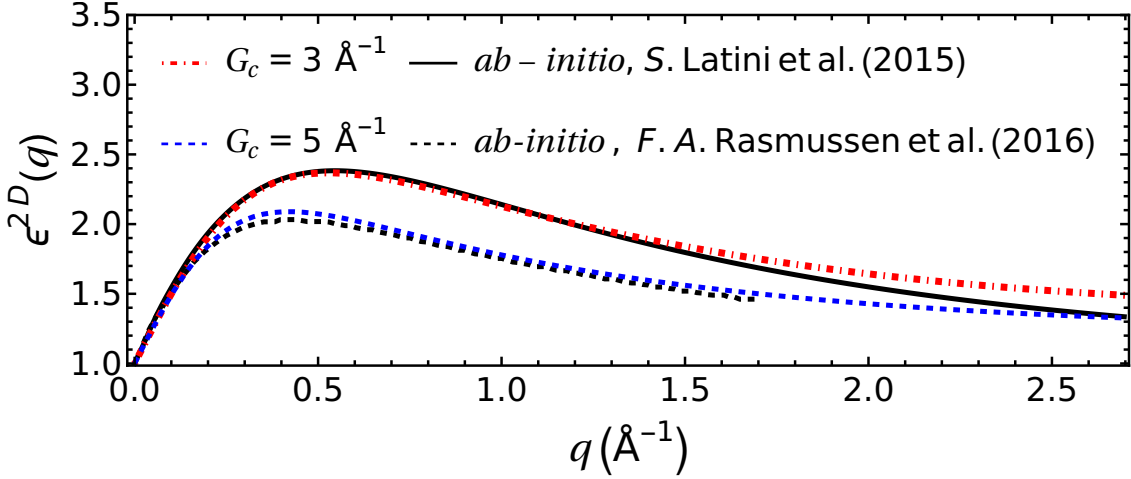


Figure S3: Macroscopic 2D dielectric function for monolayer hexagonal boron nitride obtained in this work, in comparison with *ab initio* predictions from the literature. To get the dashed red curve, we applied a cutoff  $G_c^\epsilon = 3 \text{ \AA}^{-1}$  for the reciprocal lattice vectors, corresponding to an energy cutoff of  $E_{G_c^\epsilon} = \hbar^2(G_c^\epsilon)^2/2m_e \approx 135 \text{ eV}$ , and used the model from CRYSTAL with the HSE06 exchange–correlation functional from the main text. The cutoff applied by Latini *et al.* in Ref. [7] was of 150 eV, which resulted in the continuous black curve. The work by Rasmussen *et al.* in Ref. [10] does not disclose the cutoff energy used to reproduce the dashed black curve, but we could reproduce it (up to some small disagreements) with a cutoff of  $G_c^\epsilon \approx 5.01 \text{ \AA}^{-1}$ , corresponding to including only 8 non-null reciprocal lattice vectors. The result is shown in the blue dashed curve. Our curves were obtained using the strict 2D formalism of the microscopic dielectric function.

We give a word on how different models might result in similar values for the screening parameter  $r_0$ , now for  $\text{MoS}_2$ . Estimated values for  $r_0$  are presented in the last column of Table S.4. Two models were used, the CRYSTAL one from the main text, and a Wannier model whose DFT bands were computed with the QuantumESPRESSO code [3], followed by a Wannier interpolation using the WANNIER90 package [8]. The output files from WANNIER90 can be converted into input files for the XATU library [11] through a recently developed interface. The value from CRYSTAL is comparable to the value coming from the Wannier model. A small disparity can however be identified. It is justifiable, since these two models provide slightly different band structures, particularly with distinct bandgaps. Still, both values for  $r_0$  are well within the *ab initio* range of values of 30–40 Å reported in the literature [2].

Finally, we compare the numerical dielectric functions obtained using the quasi-2D (Q2D) formalism of the main text using the two different models for  $\text{MoS}_2$ . They are displayed in Fig. S4 below, together with the *ab initio* result from the main text. We note a very good agreement between our curves and

Table S2: Comparison of the value obtained for the screening parameter among different models for MoS<sub>2</sub>. one model in the CRYSTAL one from the main text, while the other model consists of a model Hamiltonian in a basis of localized Wannier functions.

Model	Bandgap $\Delta$ (eV)	$r_0$ (Å)
CRYSTAL	2.08	35.8
Wannier	2.57	31.57

the *ab initio* one. Quite curiously, the curve obtained using the Wannier model replicates the high- $q$  behavior of the dielectric response better than the CRYSTAL model does, when compared to the black curve. Conversely, the CRYSTAL model replicates the low- $q$  dielectric response better than the Wannier model. All in all, there is a very good qualitative agreement among the three curves.

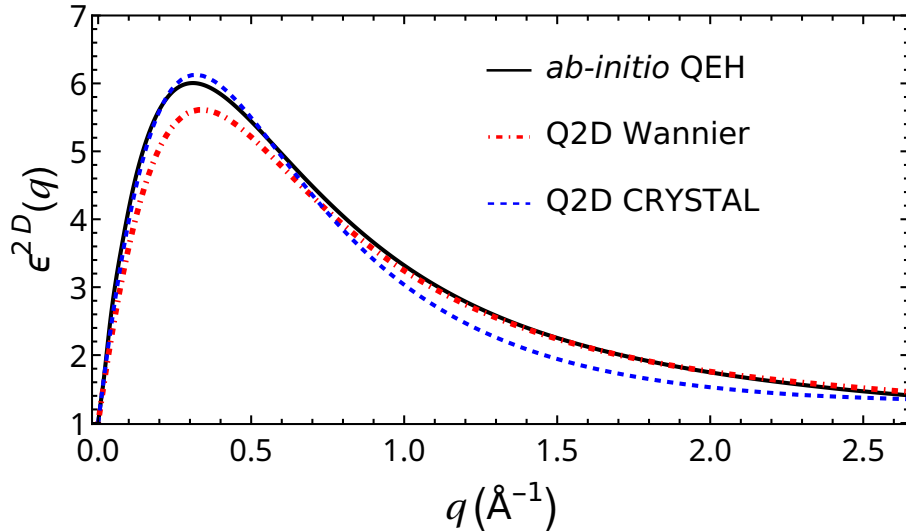


Figure S4: Macroscopic 2D dielectric function for monolayer MoS<sub>2</sub> obtained in this work, in comparison with *ab initio* predictions from the literature. We included 5 reciprocal lattice vectors including the null vector, just as in the main text (see Fig. 4b therein). The dashed blue curve corresponds to the CRYSTAL model from the main text, while the dashed red curve corresponds to the Wannier model used in this SI. The black curve was obtained using the QE code [1], and is the same from Fig. 4b in the main text.

## References

- [1] Kirsten Andersen, Simone Latini, and Kristian S. Thygesen. Dielectric genome of van der Waals heterostructures. *Nano Letters*, 15(7):4616–4621, 2015.
- [2] T. C. Berkelbach, M. S. Hybertsen, and D. R. Reichman. Theory of neutral and charged excitons in monolayer transition metal dichalcogenides. *Physical Review B*, 88(4):045318, 2013.
- [3] Paolo Giannozzi, Stefano Baroni, Nicola Bonini, Matteo Calandra, Roberto Car, Carlo Cavazzoni, Davide Ceresoli, Guido L Chiarotti, Matteo Cococcioni, Ismaila Dabo, et al. Quantum espresso: a modular and open-source software project for quantum simulations of materials. *Journal of physics: Condensed matter*, 21(39):395502, 2009.
- [4] A. Guandalini, P. D’Amico, A. Ferretti, and D. Varsano. Efficient *GW* calculations in two-dimensional materials through a stochastic integration of the screened potential. *npj Computational Materials*, 9(1):44, 2023.
- [5] F. Hüser, T. Olsen, and K. S. Thygesen. How dielectric screening in two-dimensional crystals affects the convergence of excited-state calculations: Monolayer MoS<sub>2</sub>. *Physical Review B*, 88(24):245309, 2013.

- [6] Sohrab Ismail-Beigi. Truncation of periodic image interactions for confined systems. *Physical Review B*, 73(23):233103, 2006.
- [7] S. Latini, T. Olsen, and K. S. Thygesen. Excitons in van der Waals heterostructures: The important role of dielectric screening. *Physical Review B*, 92(24):245123, 2015.
- [8] Arash A. Mostofi, Jonathan R. Yates, Giovanni Pizzi, Young-Su Lee, Ivo Souza, David Vanderbilt, and Nicola Marzari. An updated version of wannier90: A tool for obtaining maximally-localised Wannier functions. *Computer Physics Communications*, 185(8):2309–2310, 2014.
- [9] R. M. Pick, M. H. Cohen, and R. M. Martin. Microscopic theory of force constants in the adiabatic approximation. *Physical Review B*, 1(2):910–920, 1970.
- [10] F. A. Rasmussen, P. S. Schmidt, K. T. Winther, and K. S. Thygesen. Efficient many-body calculations for two-dimensional materials using exact limits for the screened potential: Band gaps of MoS<sub>2</sub>, h-BN, and phosphorene. *Physical Review B*, 94(15):155406, 2016.
- [11] Alejandro José Uría-Álvarez, Juan José Esteve-Paredes, M. A. García-Blázquez, and Juan José Palacios. Efficient computation of optical excitations in two-dimensional materials with the Xatu code. *Computer Physics Communications*, 295:109001, 2024.